Structure of Dark Matter Halos

- **Dark matter halos profiles:**
  - **DM only: NFW vs. Einasto**
  - **Halo concentration: evolution with time**

- **Dark matter halos profiles: Effects of baryons**
  - **Adiabatic contraction**
  - **Cusps and cores in central regions of halos**

- **Dark matter annihilation signal**

$$\rho(r) = \frac{\rho_0 r_s^3}{r(r + r_s)^2}\,, \quad M(r) = M_{\rm vir} \times \frac{f(x)}{f(C)}\,,$$

$$f(x) \equiv \ln(1 + x) - \frac{x}{1 + x}\,, \quad x \equiv \frac{r}{r_s}\,,$$

$$C \equiv \frac{r_{\rm vir}}{r_s}\,,$$

$$r_{\rm vir}(M_{\rm vir}) = 443\ h^{-1}\ {\rm kpc}\left(\frac{M_{\rm vir}/10^{11}\ h^{-1}\ M_\odot}{\Omega_0\,\delta_{\rm th}}\right)^{1/3}$$

$$M_{\rm vir} \equiv \frac{4\pi}{3}\,\rho_{\rm cr}\,\Omega_0\,\delta_{\rm th}\,r_{\rm vir}^3\,.$$

$$V_{\rm max}^2 = \frac{GM_{\rm vir}}{r_s} \times \frac{f(2)}{2f(C)}\,, \quad f(2) \approx 0.432\,,$$

$$M(r) = \frac{r_s\,V_{\rm max}^2}{G} \times \frac{2f(x)}{f(2)}\,, \quad \Omega^2(r) = \frac{V_{\rm max}^2}{r_s^2} \times \frac{2f(x)}{x^3 f(2)}\,,$$

$$V_{\rm esc}^2 = -2\phi(r) = 4V_{\rm max}^2 \times \frac{\ln(1 + x)}{x f(2)}\,,$$

NFW:

$$\Omega^2(r) = \frac{GM}{r^3} = \frac{GM_{\rm vir}}{r_s^3 f(C)} \times \frac{f(x)}{x^3}\,,$$

$$\phi(r) = -\frac{GM_{\rm vir}}{r_s\,f(C)} \times \frac{f(x) + x/(1 + x)}{x}$$

Einasto:

$$\rho_{\rm Ein}(r) = \rho_0 \exp\left(-\frac{2}{\alpha}\left[x^\alpha - 1\right]\right)\,, \quad x \equiv \frac{r}{r_{-2}}$$

the radius r_{-2} is the characteristic radius of the halo where the logarithmic slope of the density profile d log(ϱ)/d log(R) is equal to -2.

$$f_E(x,\alpha) = e^{\frac{2}{\alpha}} \int_0^x x^2 e^{-\frac{2}{\alpha}x^\alpha}\,dx,$$

$$x \equiv \frac{r}{r_{-2}}, \quad C = \frac{R_{\rm vir}}{r_{-2}}.$$

Densities and velocities at large distances

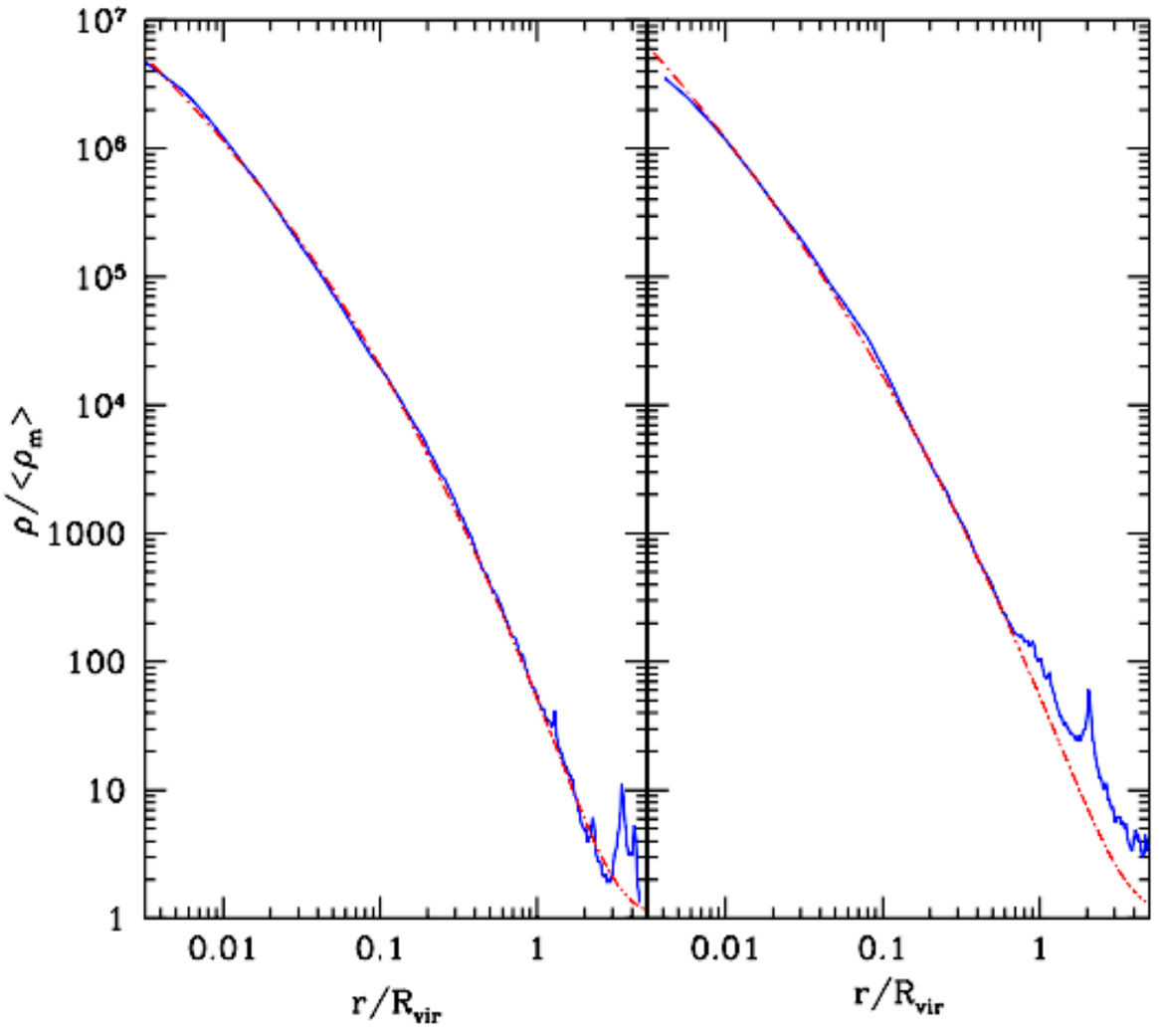

Fig. 1.— Dark matter density profiles of two dark matter halos (full curves) in the simulation Box20. The halos have virial masses of $1.4 \times 10^{12} h^{-1} M_\odot$ (left panel) and $2.6 \times 10^{11} h^{-1} M_\odot$ (right panel). The larger halo has a neighbour at 3.5 R_{vir} which is the halo on the right panel. This smaller halo is responsible for the spike at large radii in the density profile. In turn, the halo on the right panel has its own smaller neigbour at $2R_{vir}$ observed as a spike and an extended bump in the density profile. The dashed curves show the 3D Sersic profiles. The halo density profiles extend well beyond the formal virial radius with the Sérsic profile providing remarkably good fits.

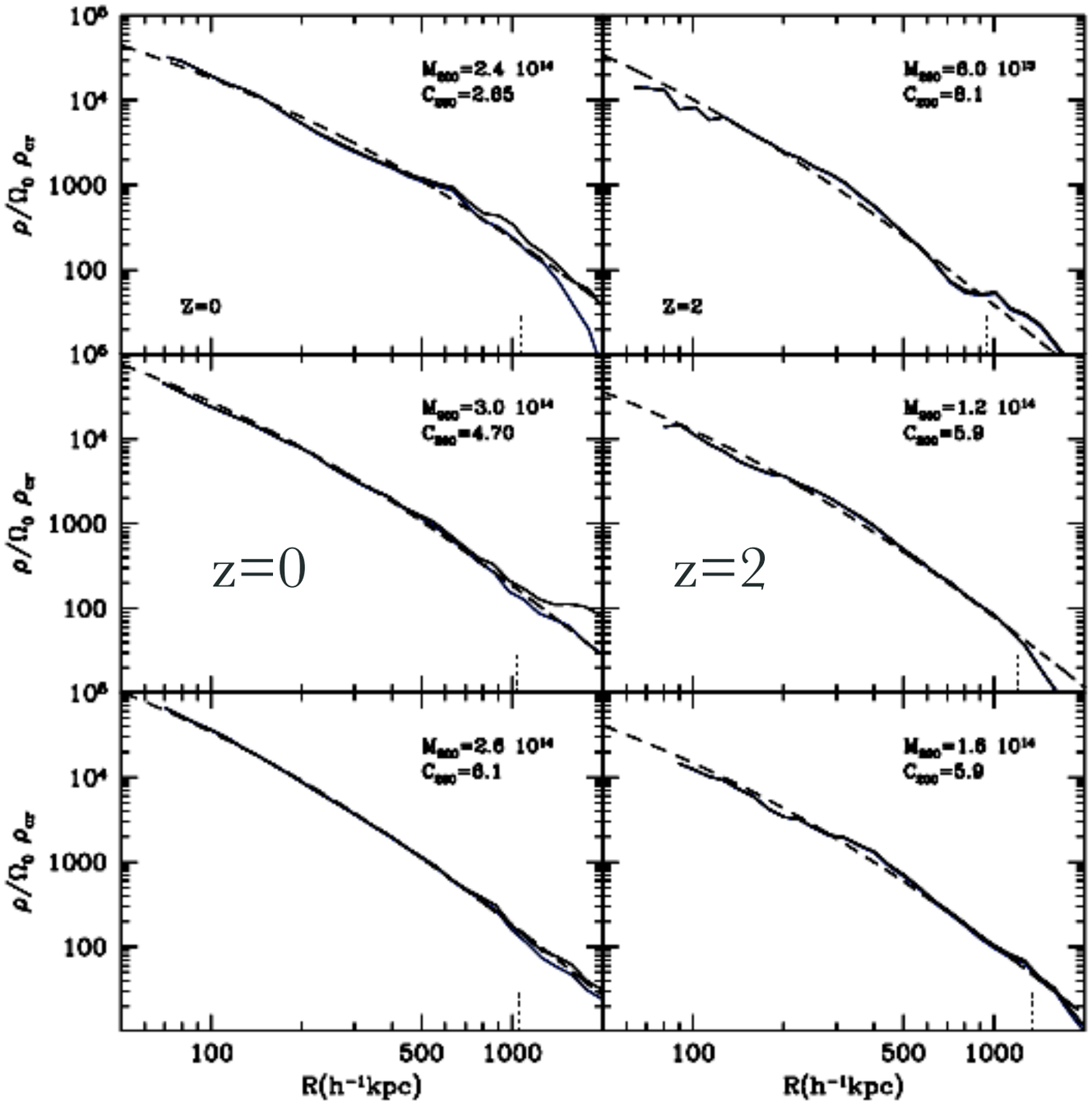

Figure 3. Examples of density profiles for cluster-size haloes (full curves) and their fits (dashed curves) using concentrations obtained with the ratios of the maximum circular velocity V_{max} to the halo velocity V_{200}. Panels on the left are for redshift $z = 0$ and the right-hand panels are for $z = 2$. Each panel shows two full curves: the density profile of all particles (upper curve) and only bound particles (lower curve). Vertical dotted lines show the outer radius of bound particles.

Dark matter profiles

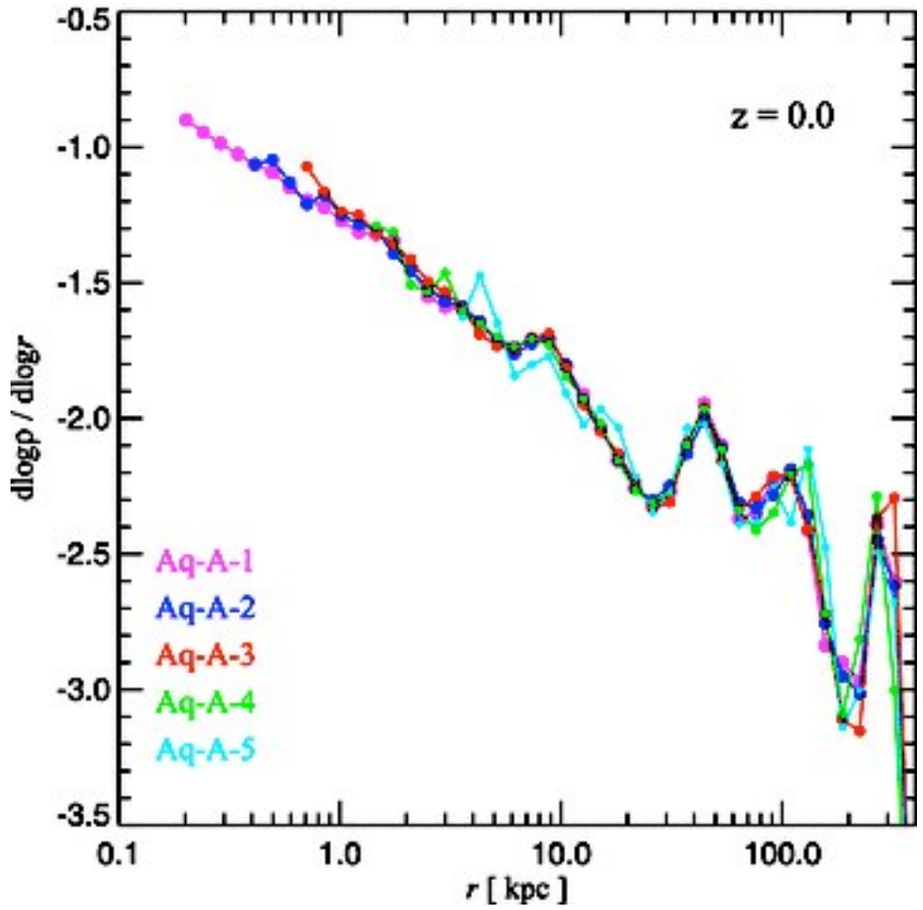

Aquarius simulation. Springel et al 2008. WMAP-1

Central slope is very close to -1

For normal galaxies it does not matter: baryons dominate in those regions and affect DM

Stadel etal 2009

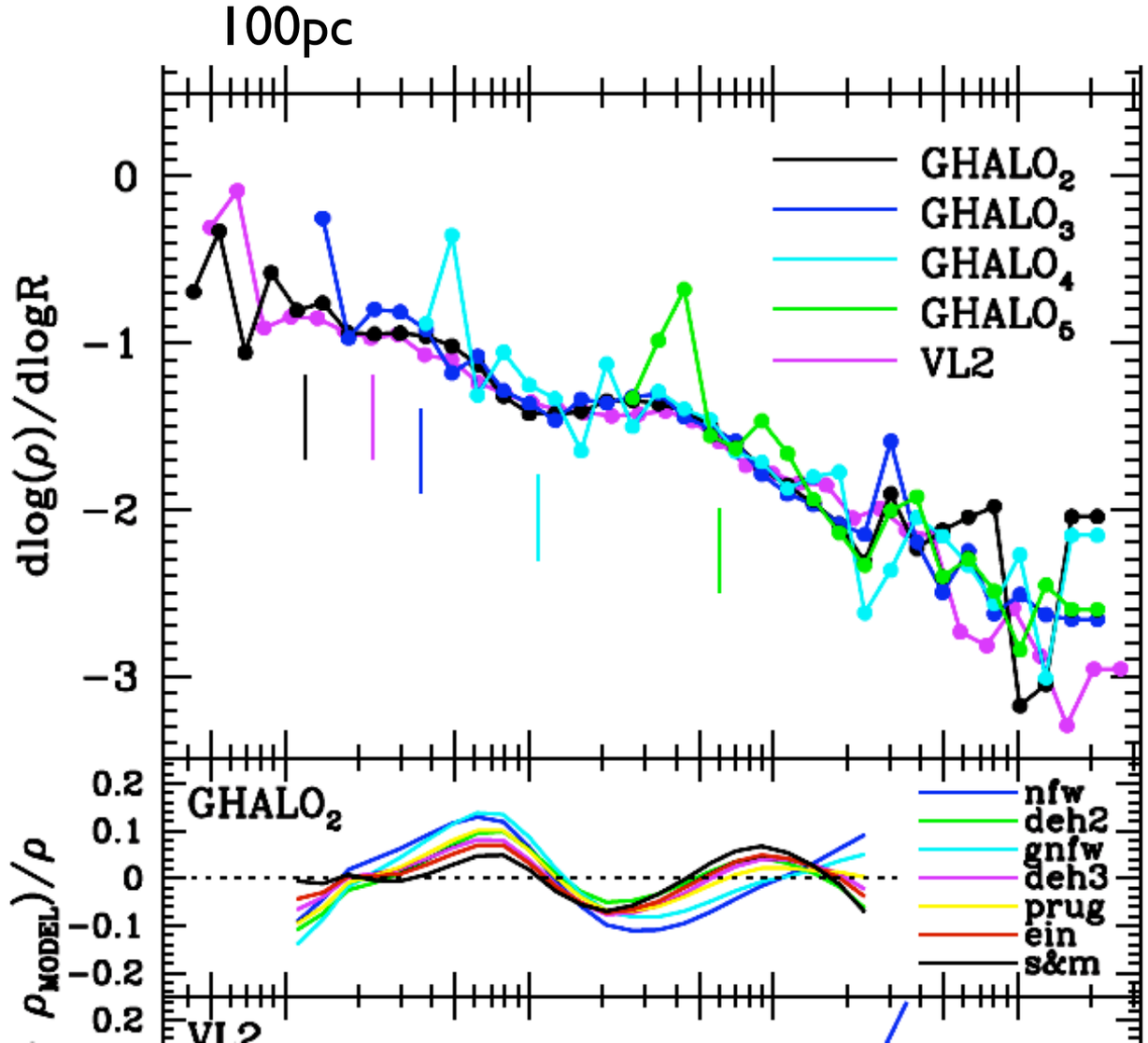

Einasto

$$\rho_{-2} = \rho_s/4$$

$$r_{-2} = r_s.$$

$$\alpha = 0.2$$

$$\ln(\rho_\alpha/\rho_{-2}) = (-2/\alpha)[(r/r_{-2})^\alpha - 1].$$

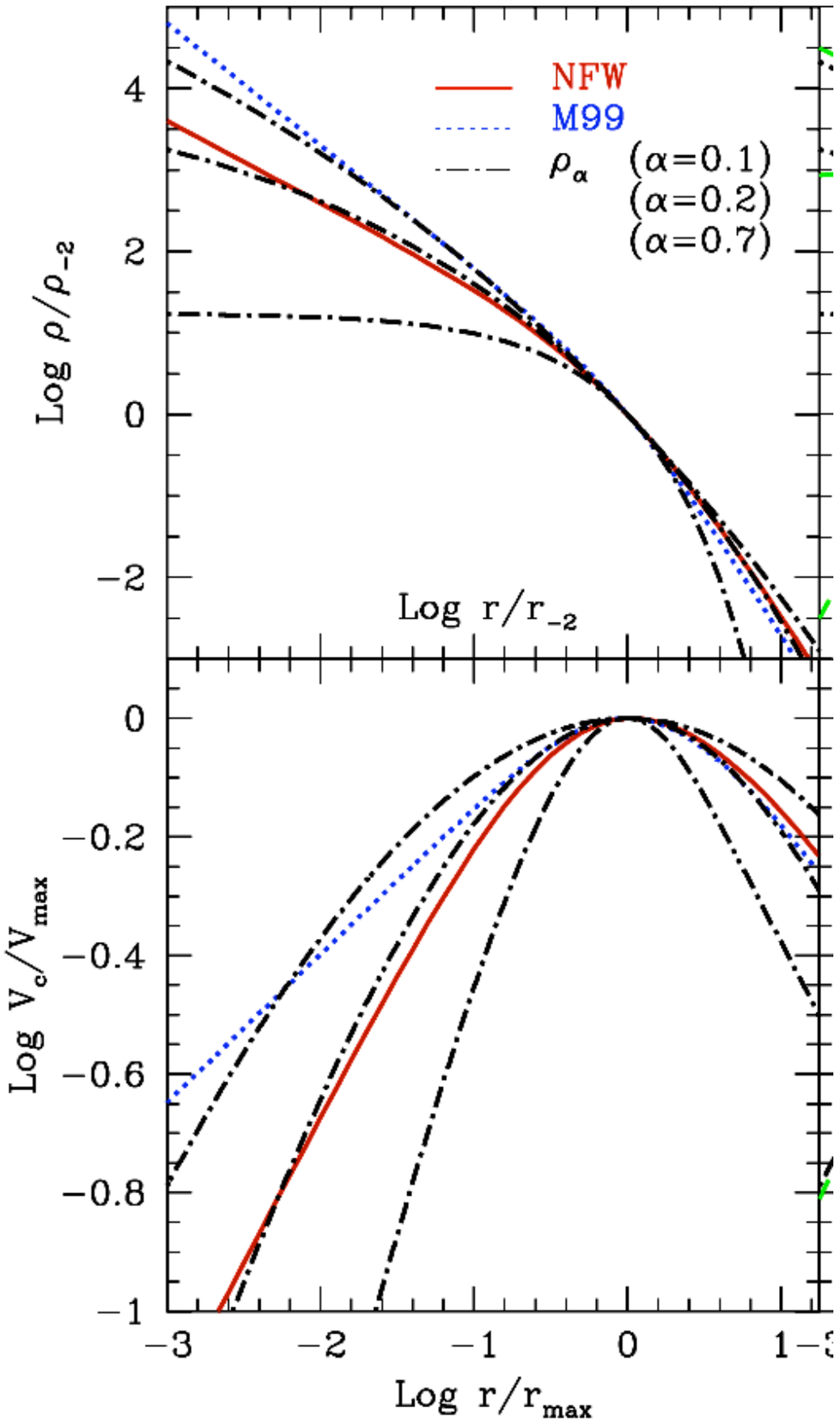

Navarro etal 2004

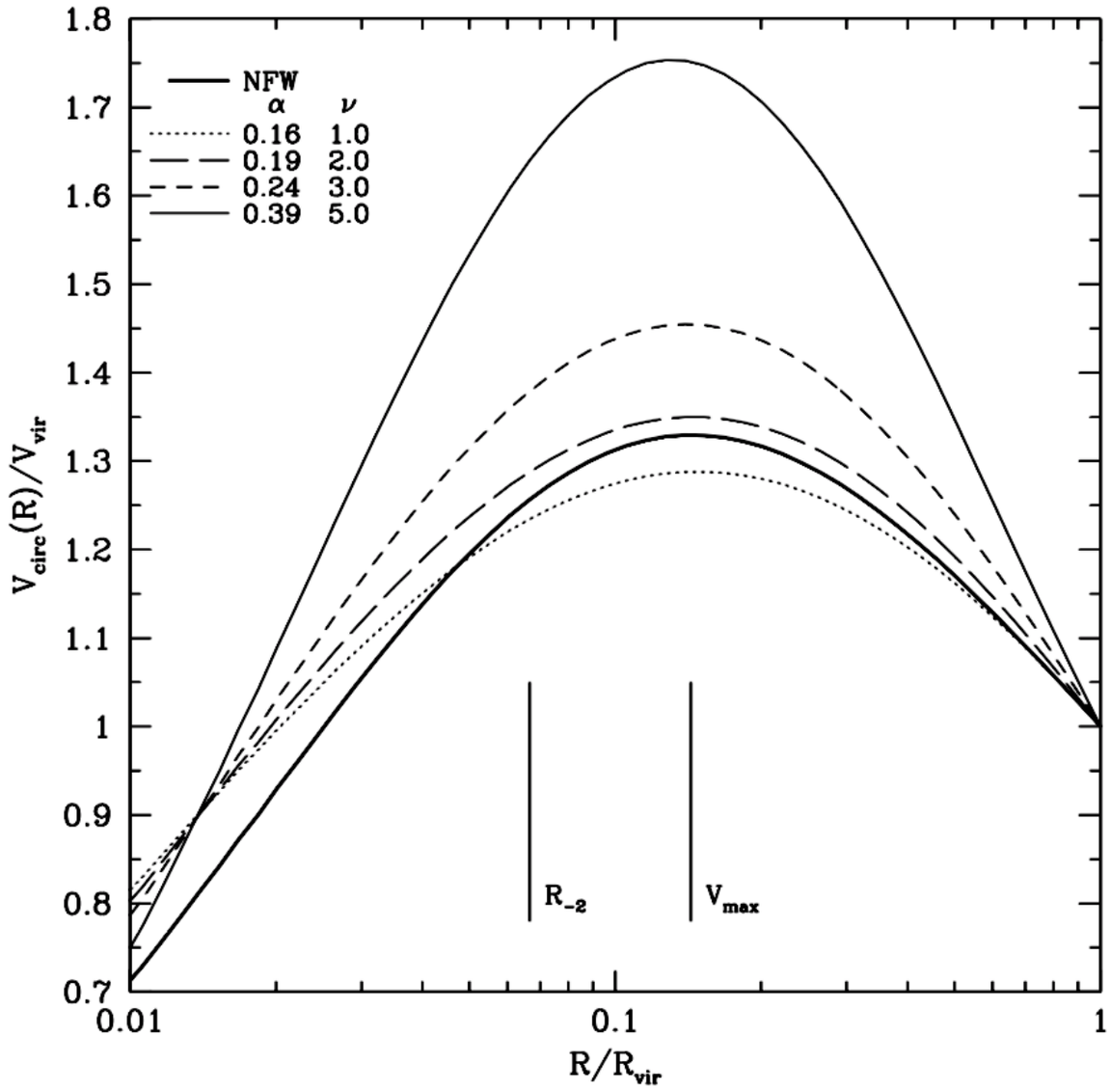

Comparison the NFW halo profile with the Einasto profiles with different parameters α. Halos where fixed to have the same virial mass, and the same radius r_{-2} where the slope of the density profile is equal to d log(ϱ)/d log(R) = –2. In cosmological simulations the parameter α depends of the peak height ν with larger ν (and, thus, larger mass M) corresponding to larger parameters α. The ratio of the maximum circular velocity to the virial velocity V_{circ}/V_{vir} is related with halo concentration for any profile.

Density profiles of halos with mass $M_{200} \approx 1.2 \times 10^{14} h^{-1} M_\odot$ at z = 1.5 (full curves). Dot-dashed curves show Einasto fits, which have the same virial mass as halos in the simulation. The NFW profiles (dashed curves) do not provide good fits to the profiles and significantly depend on what part of the density profile is chosen for fits.

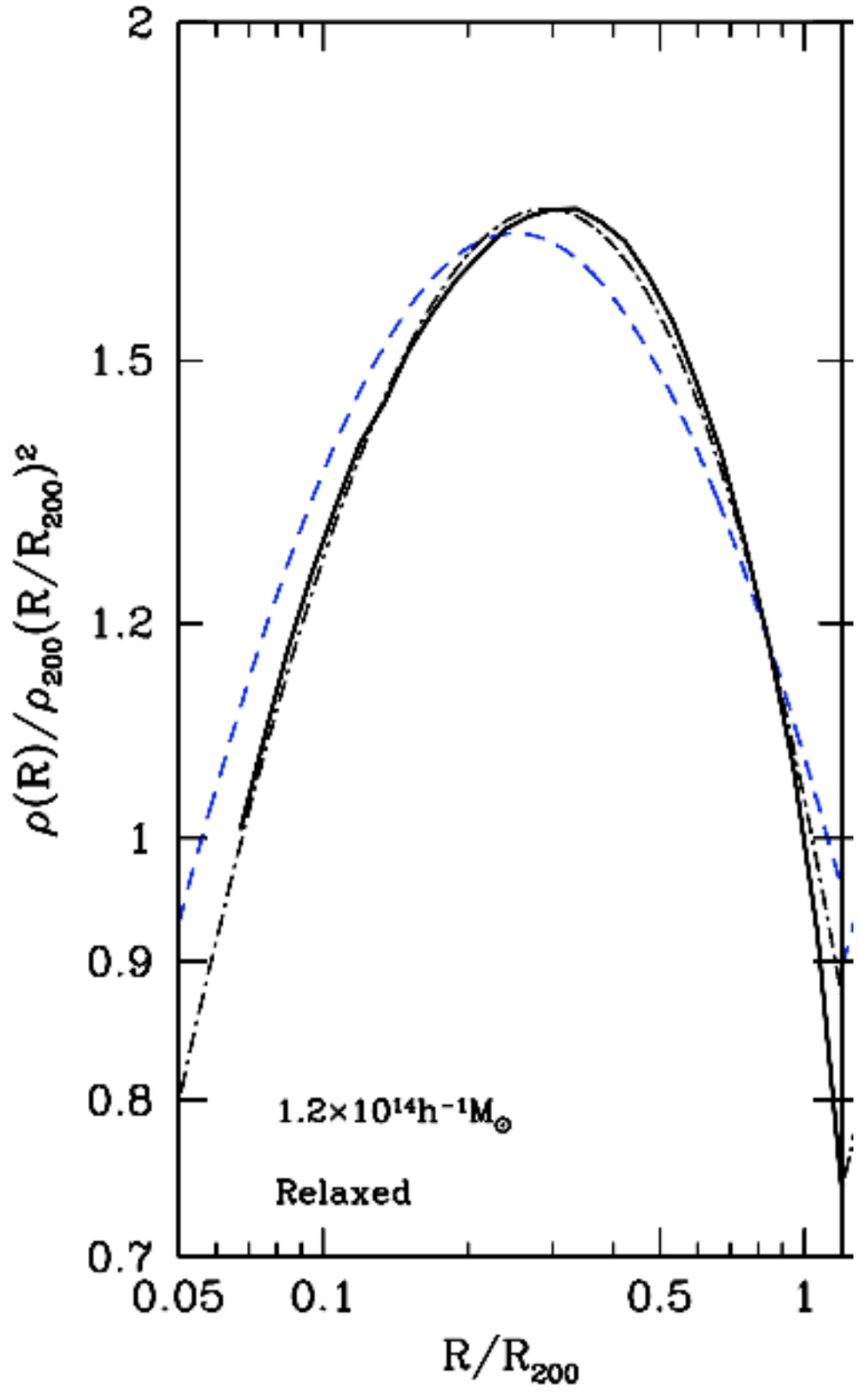

M=5x10^12

M=9x10^10

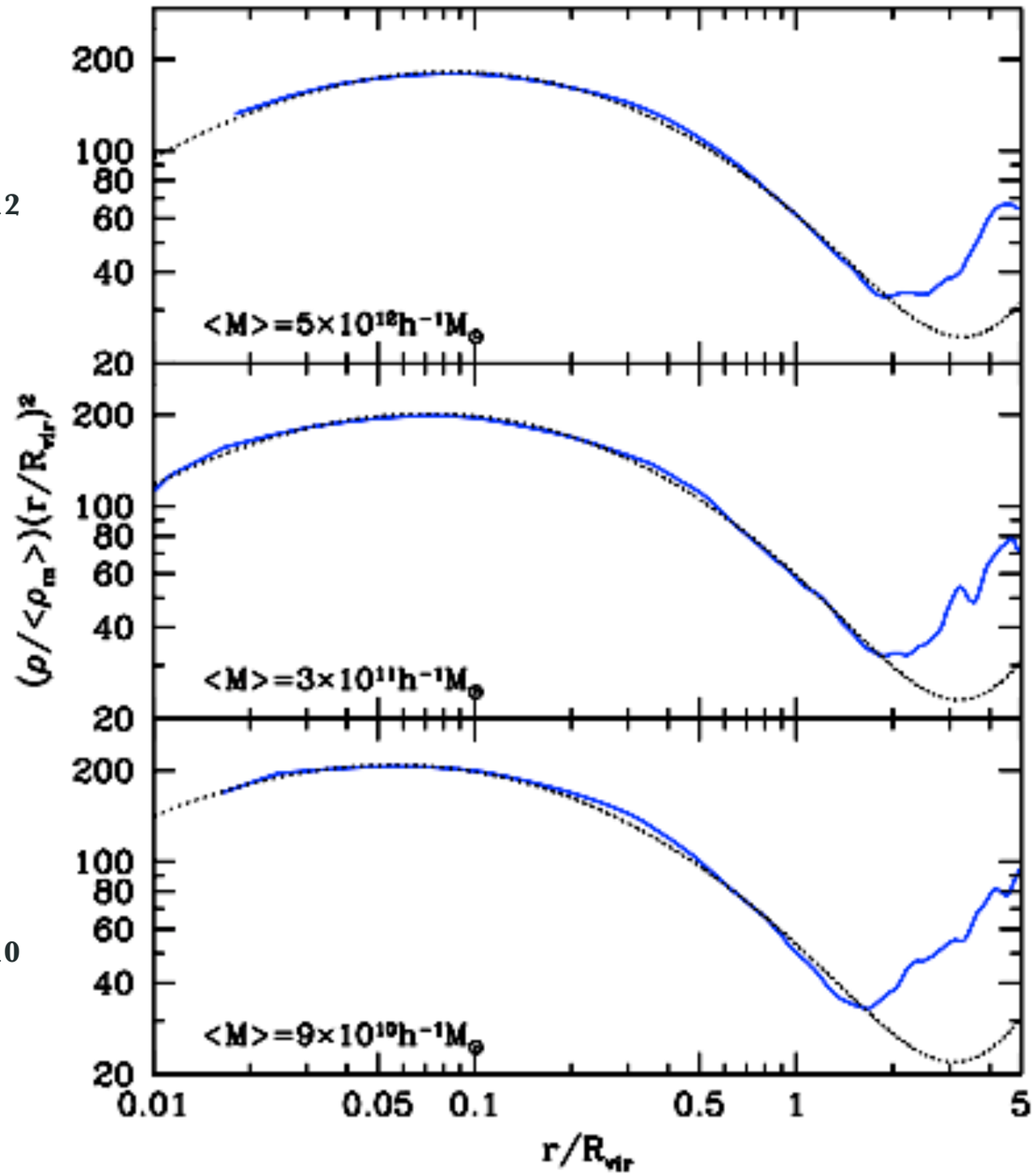

Fig. 3.— Average density profiles for halos with different virial masses. The 3D Sérsic profile provides very good fit with few percent errors within $2R_{vir}$. Even at $3R_{vir}$ the error is less than 20-30 percent. The density profiles are well above the average density of the Universe throughout all the radii.

3d Sersic = Einasto

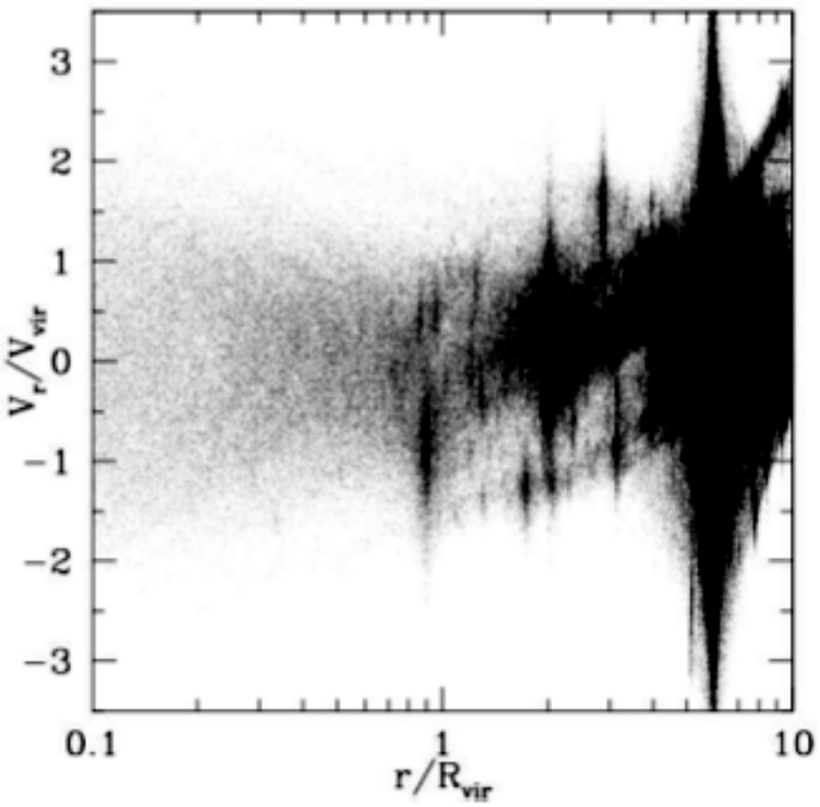

Phase-space diagram for the particles in dark matter halos

Mvir =3 10^{11}Msun

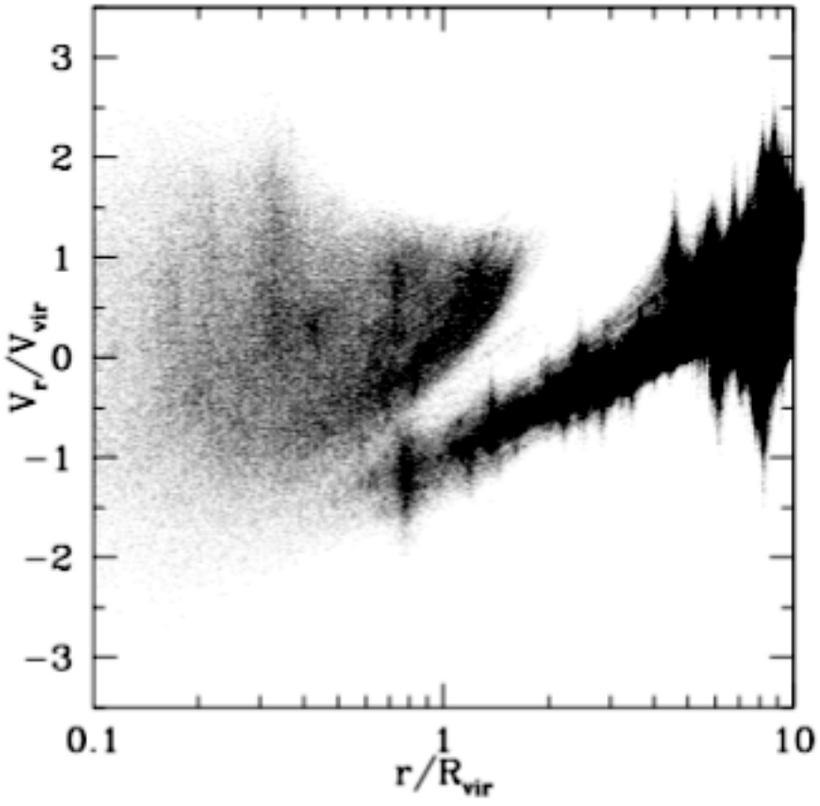

Mvir =1.5 10^{15}Msun

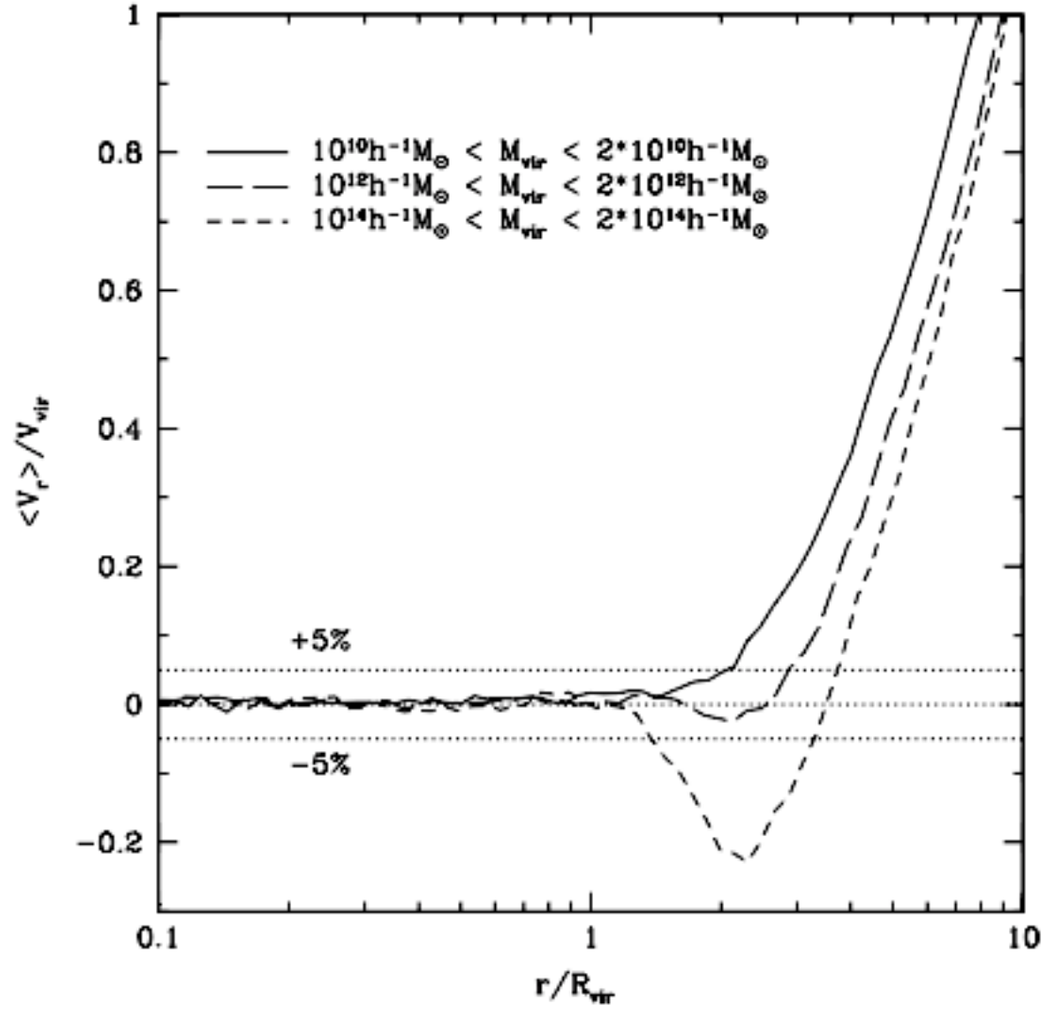

Figure 4. Mean radial velocity for three different mass bins. The profiles were obtained by averaging over hundreds of distinct haloes on each mass bin. In dotted line is shown the selected threshold delimiting the static region (5 per cent of the virial velocity). Cluster-size haloes display a region with strong infall (dashed line). On the contrary, low-mass haloes (solid line) and galactic haloes (long-dashed line) do not show infall at all but a small outflow preceding the Hubble flow.

Infall velocities on halos.

nu = peak height = δ_{cr}/σ

M=10^{13}Msun

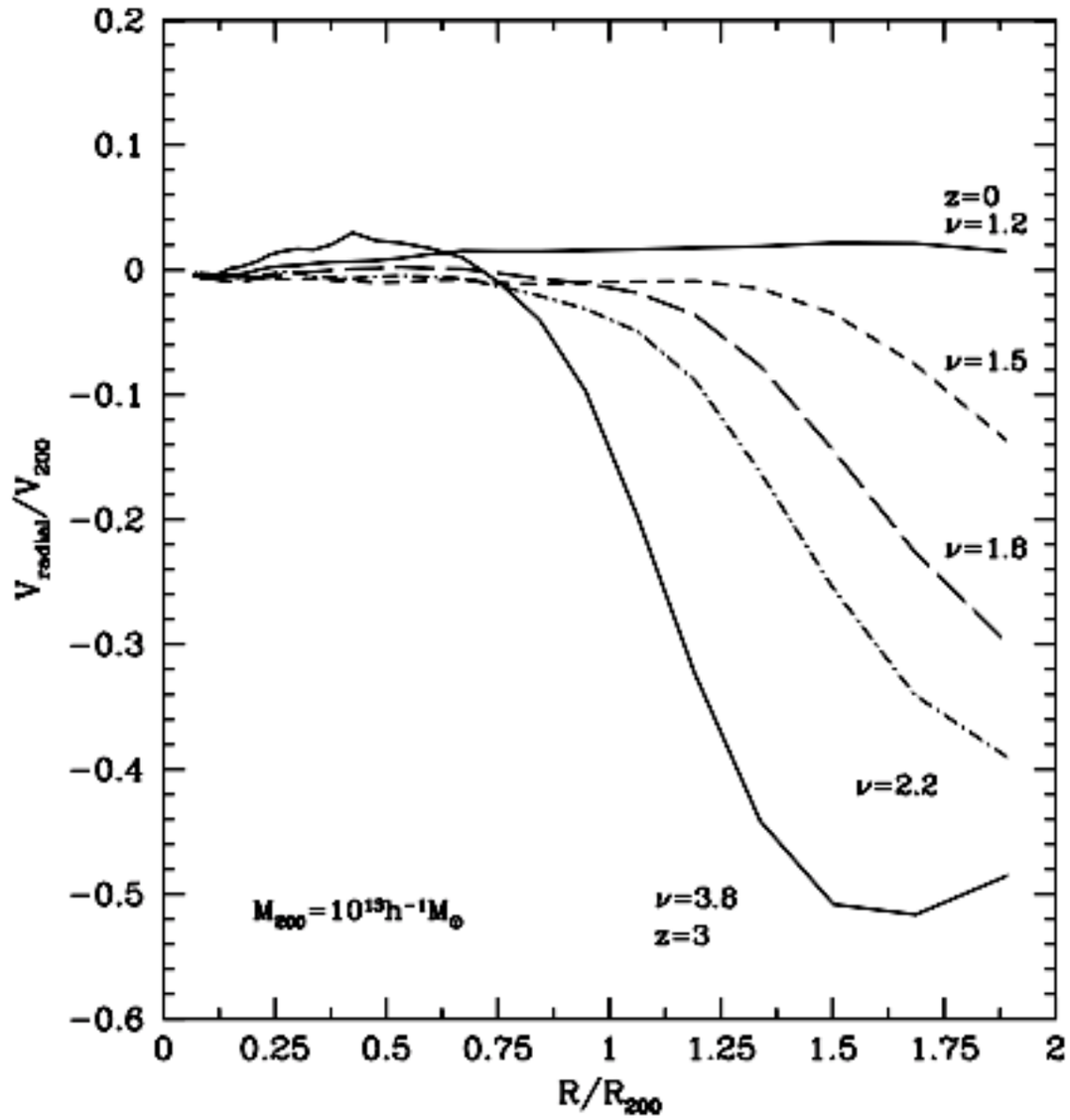

Velocity anisotropy

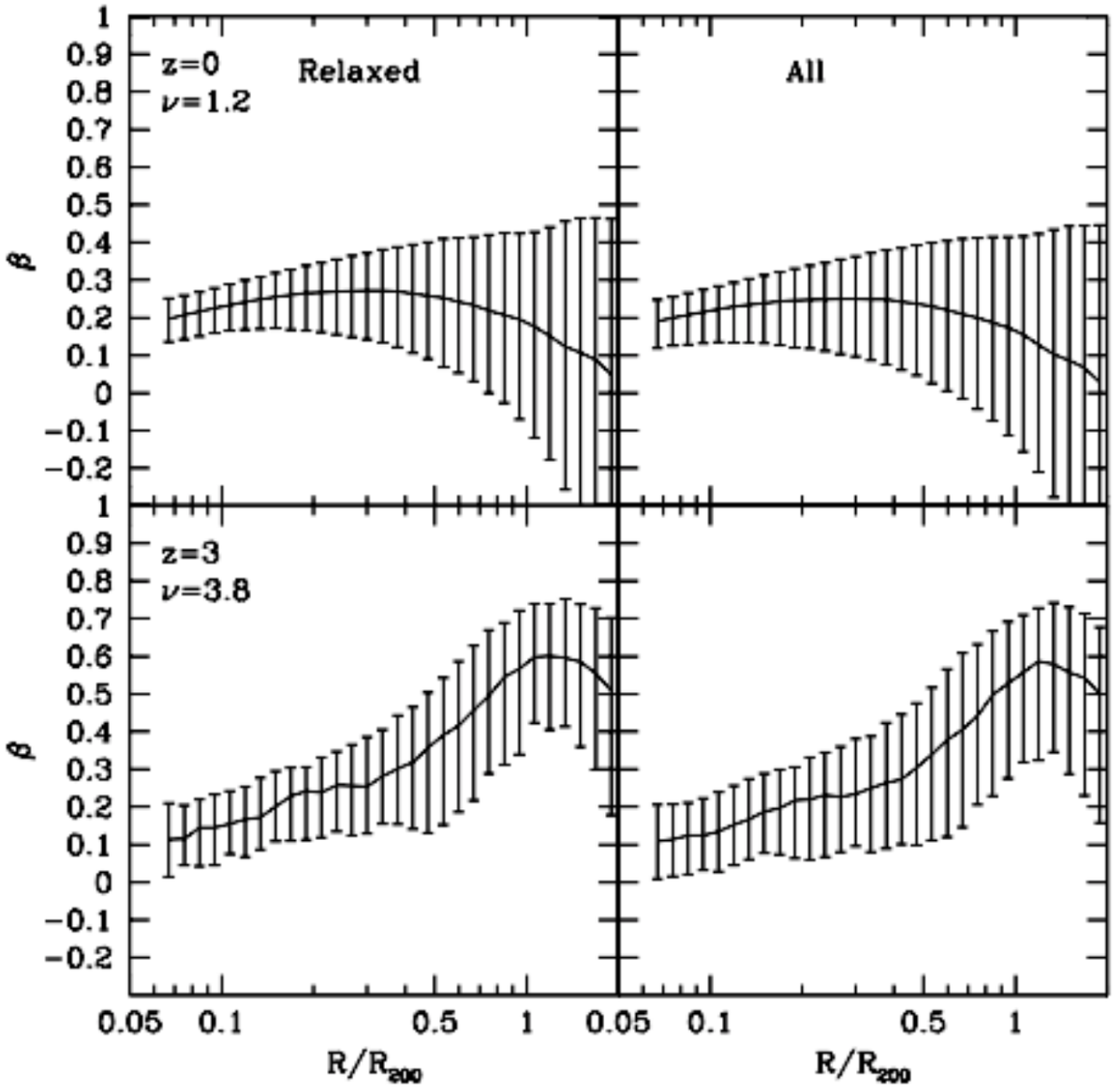

δ_{cr}/σ

M=10^{13}Msun

$$\beta = 1 - \frac{\sigma_t^2}{\sigma_r^2},$$

where σ_r^2 is the radial velocity dispersion and σ_t^2 is the tangential velocity dispersion.

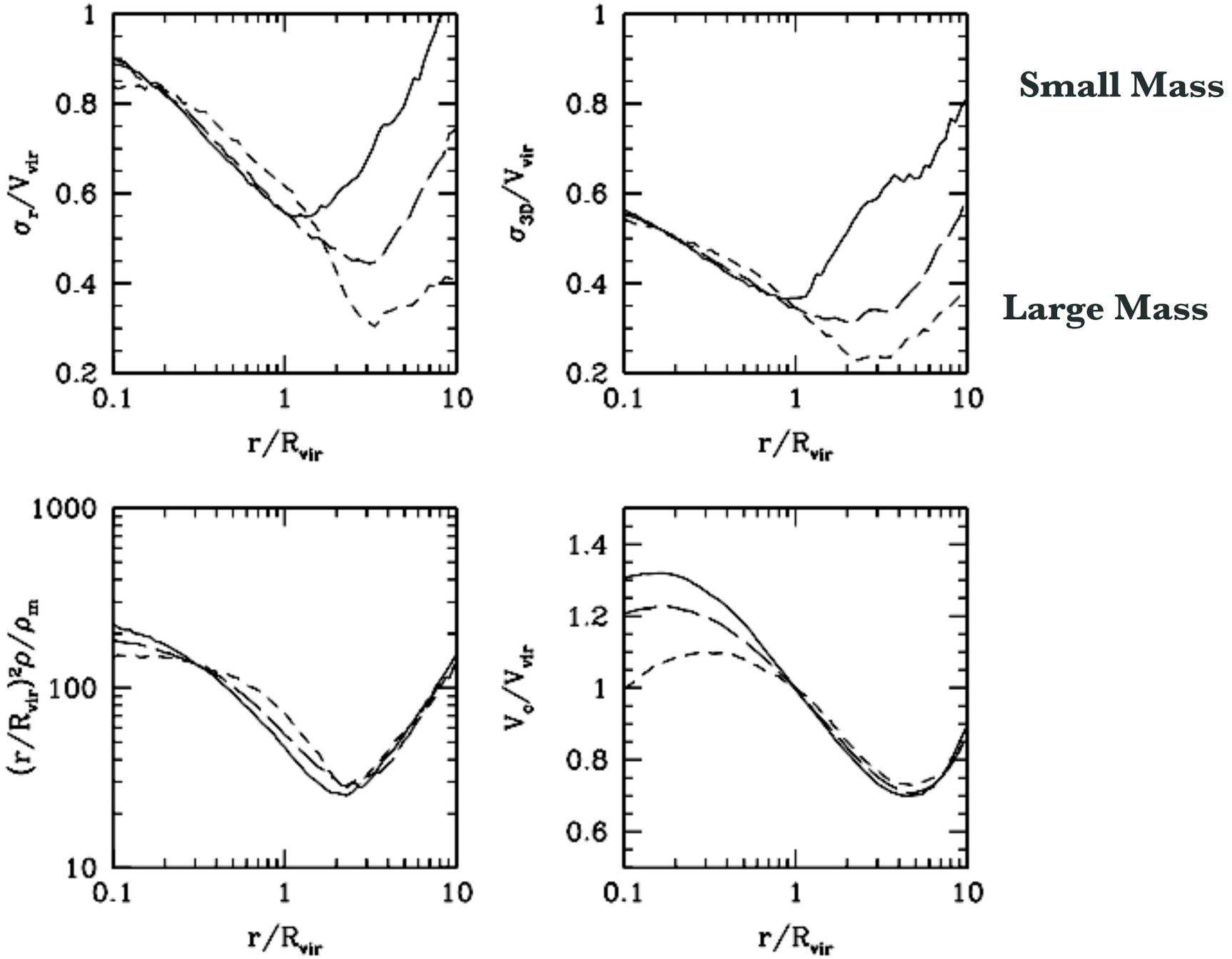

Figure 5. Median profiles for the same halo mass bins as in Figure 4. These profiles show how the behaviour of haloes depends on the halo mass. Top left panel: radial velocity dispersion. Top right: 3D velocity dispersion. Bottom left: density profile. Bottom right: Circular velocity profile. The different line styles represent the same mass bins as in Figure 4.

Halo Concentrations

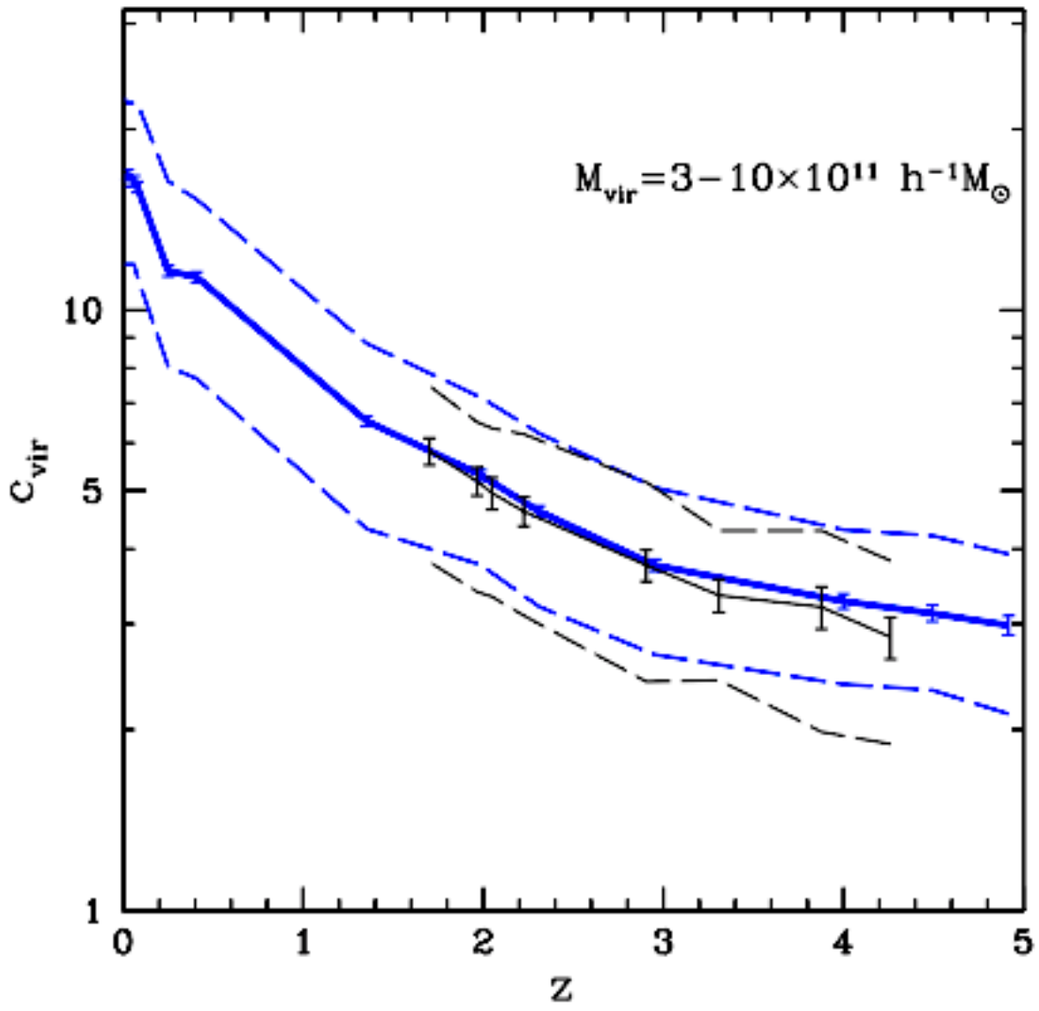

Figure 3. Convergence test for $c_{\rm vir}$ evolution and scatter. Shown is a comparison of $M_{\rm vir} = 3-10\times10^{11}h^{-1}M_\odot$ haloes simulated using our main simulation (thick lines) and a second simulation with 8 times the mass resolution (thin lines). The solid lines and errors reflect the median and Poisson uncertainty respectively. The dashed lines reflect the estimated intrinsic scatter. There is no evidence for significant deviations in either the measured median or scatter as the mass resolution is increased.

- Main trend with redshift

for a fixed halo mass

$$c_{\rm vir}(a) \propto a.$$

$$C \equiv \frac{r_{\rm vir}}{r_s},$$

$$r_{\rm vir}(M_{\rm vir}) = 443\ h^{-1}\ {\rm kpc}\left(\frac{M_{\rm vir}/10^{11}\ h^{-1}\ M_\odot}{\Omega_0\,\delta_{\rm th}}\right)^{1/3}$$

$$M_{\rm vir} \equiv \frac{4\pi}{3}\,\rho_{\rm cr}\,\Omega_0\,\delta_{\rm th}\,r_{\rm vir}^3\ .$$

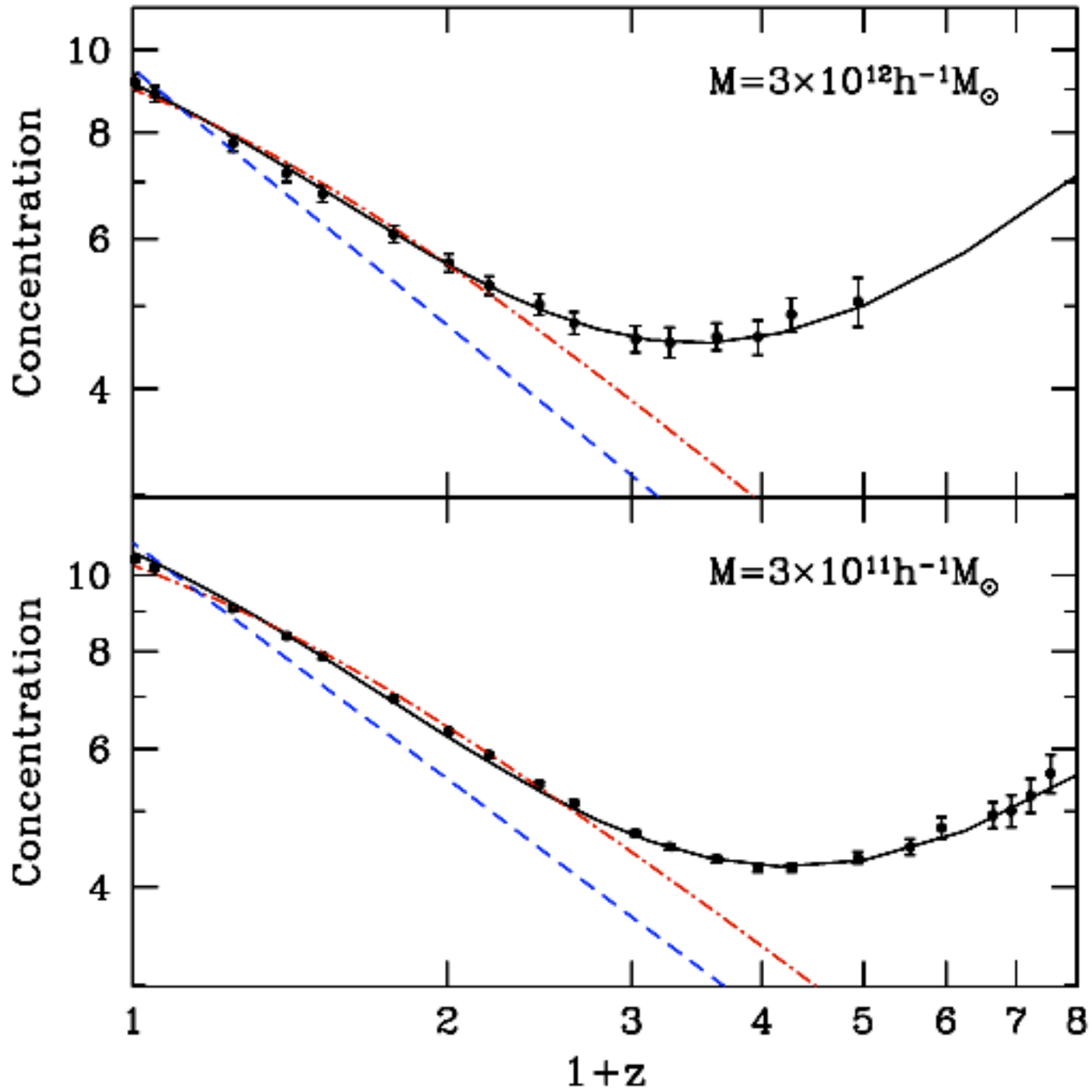

Figure 6. Evolution of halo concentration for halos with two masses indicated on the plot. The dots show results of simulations. For the reference the dashed lines show a power-law decline $c \propto (1+z)^{-1}$. Concentrations do not change as fast as the law predicts. At low redshifts $z < 2$ the decline in concentration is $c \propto \delta$ (dot-dashed curves), where δ is the linear growth factor. At high redshifts the concentration flattens and then slightly increases with mass. For both masses the concentration reaches a minimum of $c_{\rm min} \approx 4$–4.5, but the minimum happens at different redshifts for different masses. The full curves are analytical fits with the functional form of Equation (13).

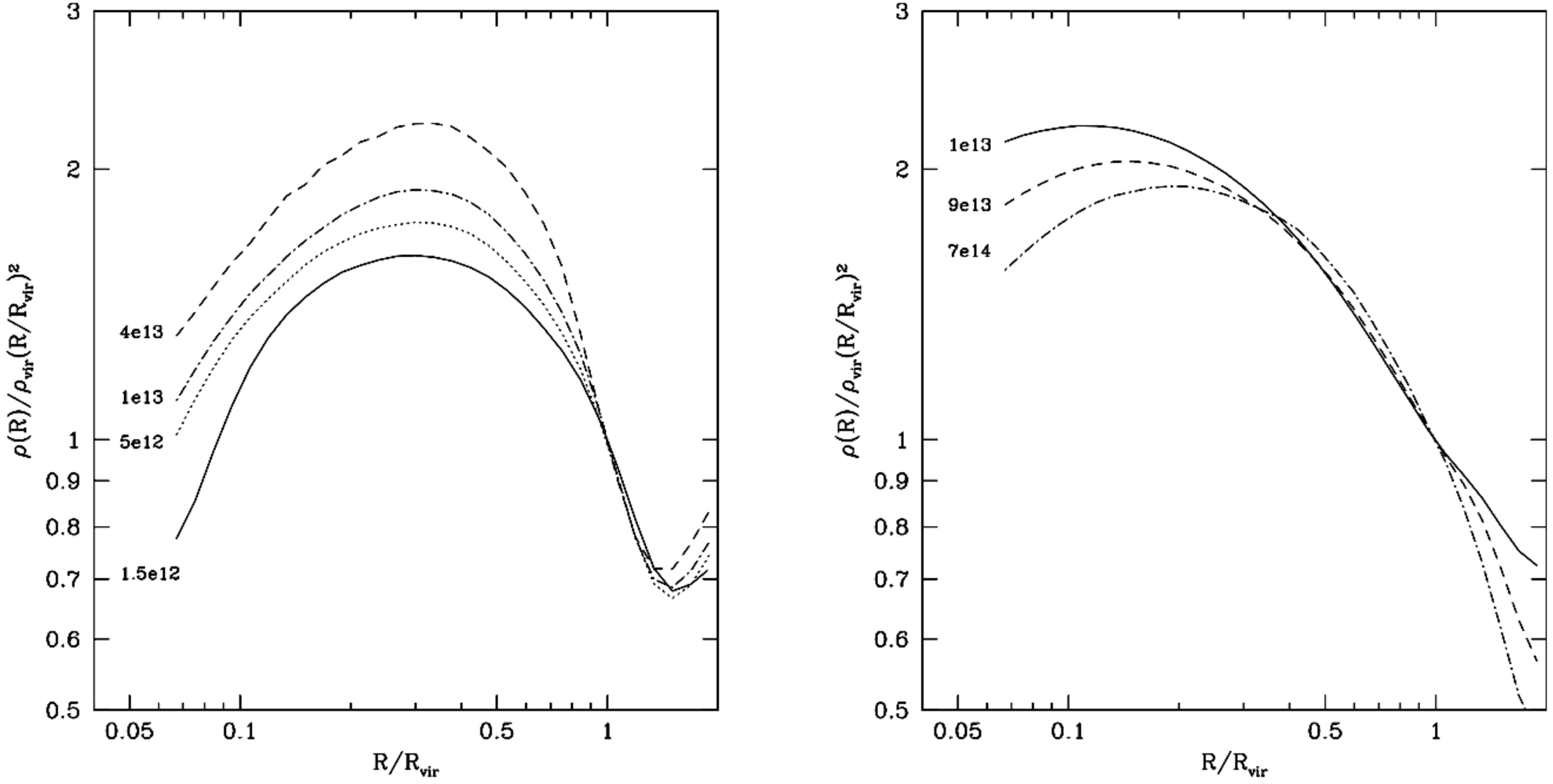

Median density profiles of relaxed halos at different redshifts and masses in N-body simulations. Profiles are normalized to have the same density at the virial radius. The left panel is for halos at z = 3: halos with larger mass are clearly more concentrated than halos with smaller masses. Similar to Einasto profiles in Figure 7, value of r_{-2} radius almost does not change with halo mass, which indicates that the increase in the concentration is mostly due to the increase in shape parameter α. The right panel shows profiles of halos at z = 0. Note that the trend with mass is different: more massive halos are less concentrated and r_{-2} radius decreases with decreasing mass.

Halo Concentration: need to know in order to get density profile

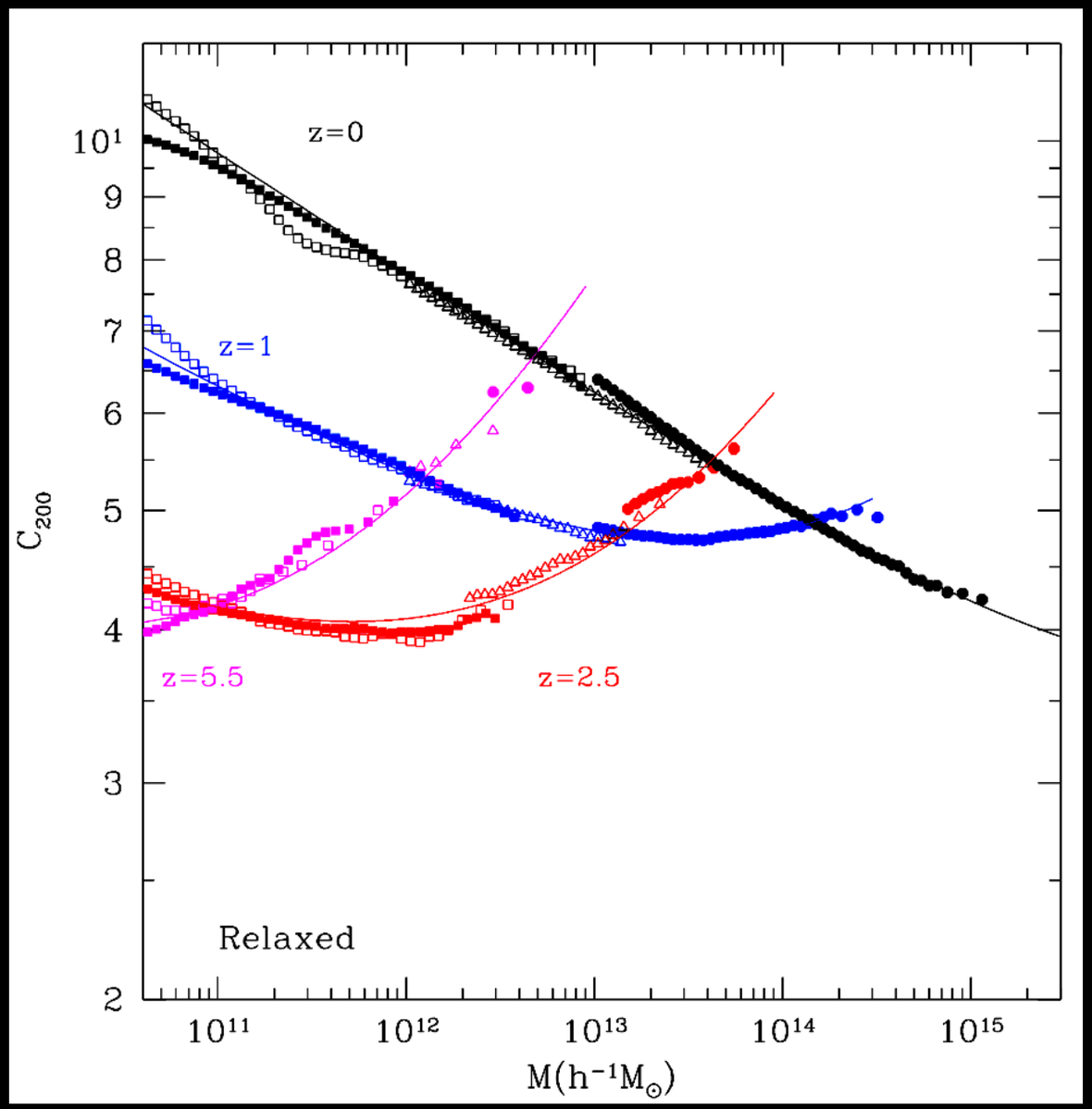

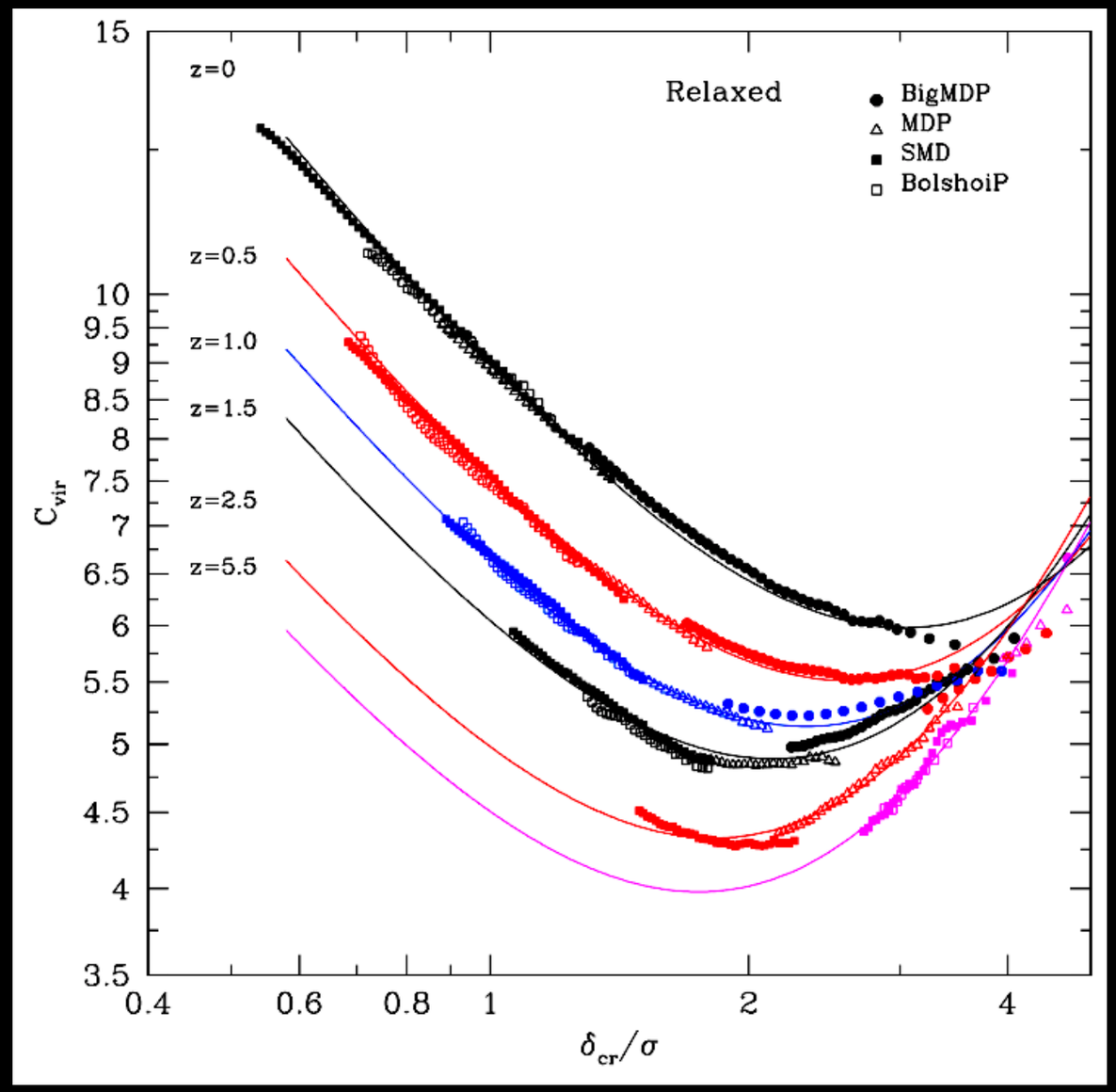

Klypin et al 2014: Gadget + ARTMultiDark suite of sims: 60G particles

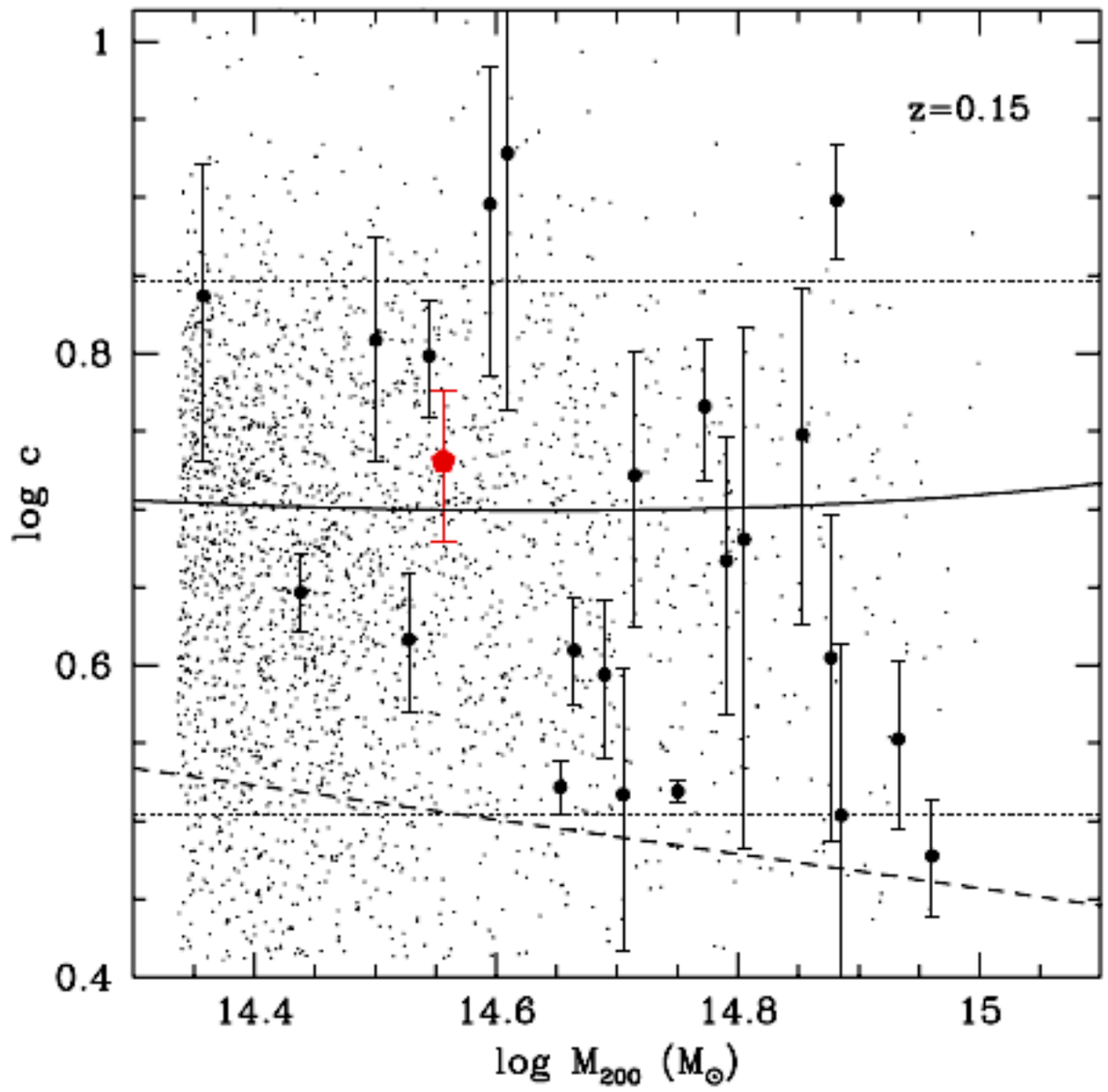

Figure 13. Comparison of observed cluster concentrations (open symbols with error bars) with the prediction of our model for median halo concentration of cluster-size haloes (full curve). Dotted lines show the 10 per cent and 90 per cent percentiles. We also show the concentrations, in the same mass interval, for all the individual simulated clusters found in the MultiDark simulation box (data points). Open circles show results for X-ray luminous galaxy clusters observed with *XMM–Newton* in the redshift range 0.1–0.3 (Ettori et al. 2010). The pentagon presents galaxy kinematic estimate for relaxed clusters by Wojtak & Łokas (2010). The dashed curve shows prediction by Macciò et al. (2008), which significantly underestimates the concentrations of clusters.

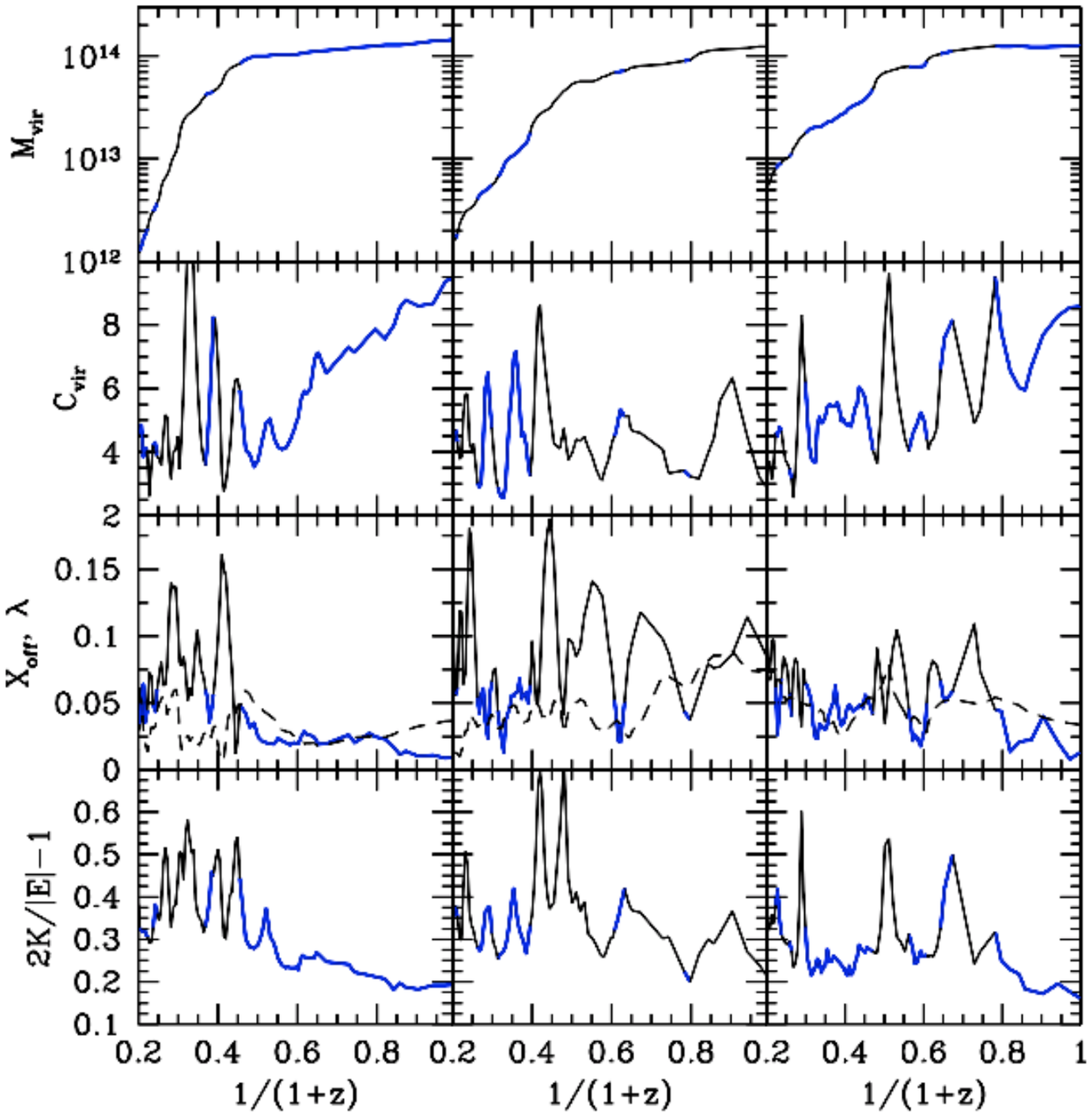

Examples of the evolution of virial mass M_{vir} , concentration C_{vir}, spin parameter λ (dashed curves in the second from the bottom panels), offset parameter X_{off} , and virial ratio 2K/|E| – 1 for 6 cluster-size halos taken from the BolshoiP simulation. Halos were selected to have $M_{vir} \approx 10^{14} h^{-1} M_{\odot}$ and be relaxed at z = 0. Thick solid (blue) parts of the curves indicate that halos are considered to be relaxed. Large variations in halo concentration are seen at high redshifts when the halo mass increases very quickly. Once the mass accretion slows down at low redshifts, halo concentration shows the tendency to increase. Major merger events, in the right panels, seen as large jumps in mass are followed by temporary increase in halo concentration. Most of these major-merger spikes in concentration are identified as happening in non-relaxed halos.

Effects of baryons: adiabatic contraction

assumptions: circular particle orbits, and conservation of the angular momentum: $M(r)r = \text{const}$, where $M(r)$ is the total mass enclosed within radius r. With these assumptions, the final DM distribution is calculated given the initial mass profiles $M_{\rm dm}(r)$, $M_b(r)$ and final baryon profile $M_b(r_f)$:

$$[M_{\rm dm}(r) + M_b(r)]r = \left[M_{\rm dm}(r) + M_b(r_f)\right]r_f.$$

the average radius along the orbit, $\bar{r}$. The orbit-averaged radius is

$$\bar{r} = \frac{2}{T_r}\int_{r_p}^{r_a} r\,\frac{dr}{v_r},$$

adiabatic contraction model based on conservation of the product of the current radius and the mass enclosed within the orbit-averaged radius:

$$M(\bar{r})r = \text{const.} \qquad (6)$$

Gnedin etal 2004

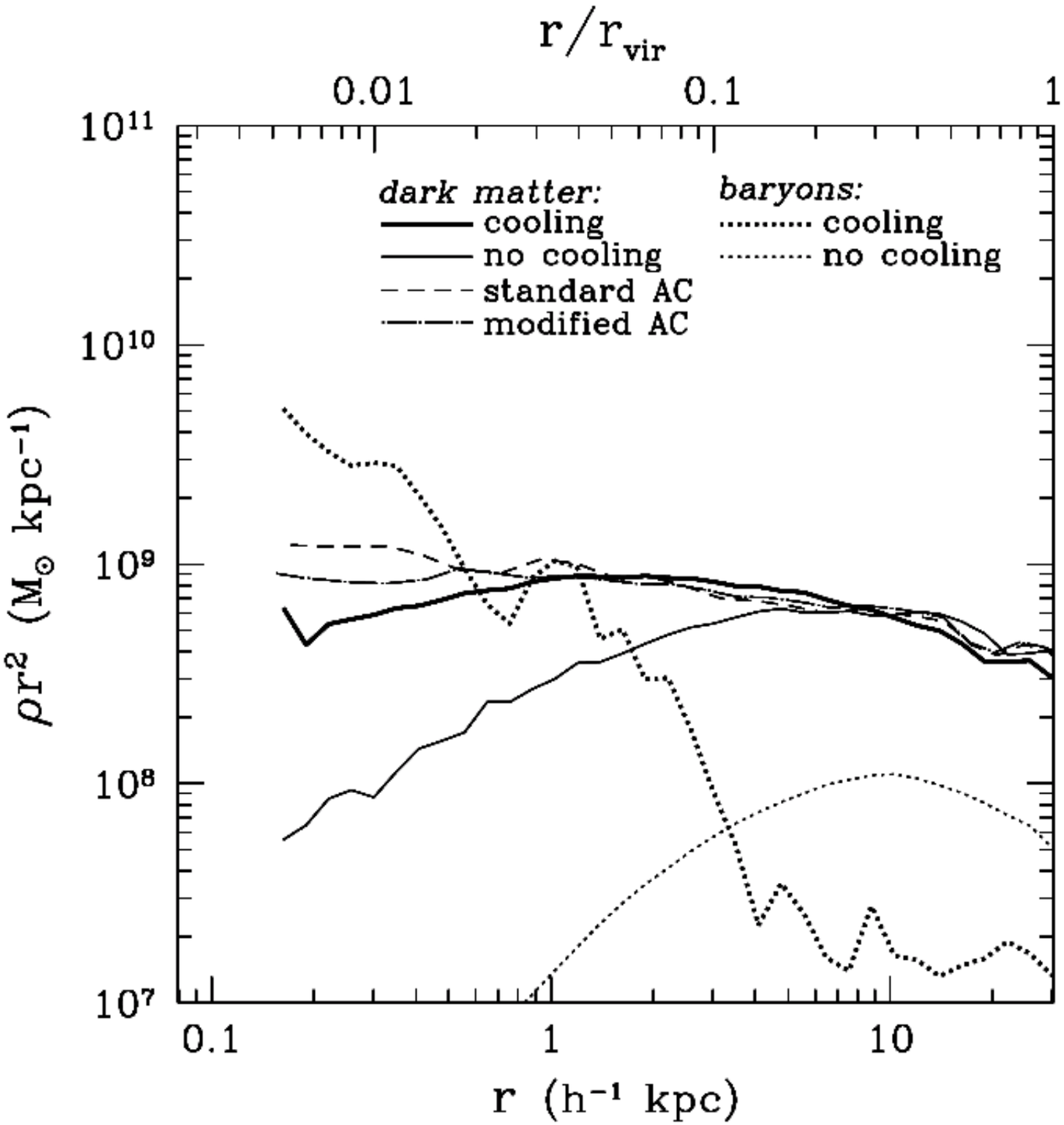

FIG. 3.—Density profile in the galaxy formation run at $z = 4$ as a function of physical radius. Lines types are as in Fig. 1. [*See the electronic edition of*

Density Profiles: Mass at ~1 kpc radius. Core-cusp problem

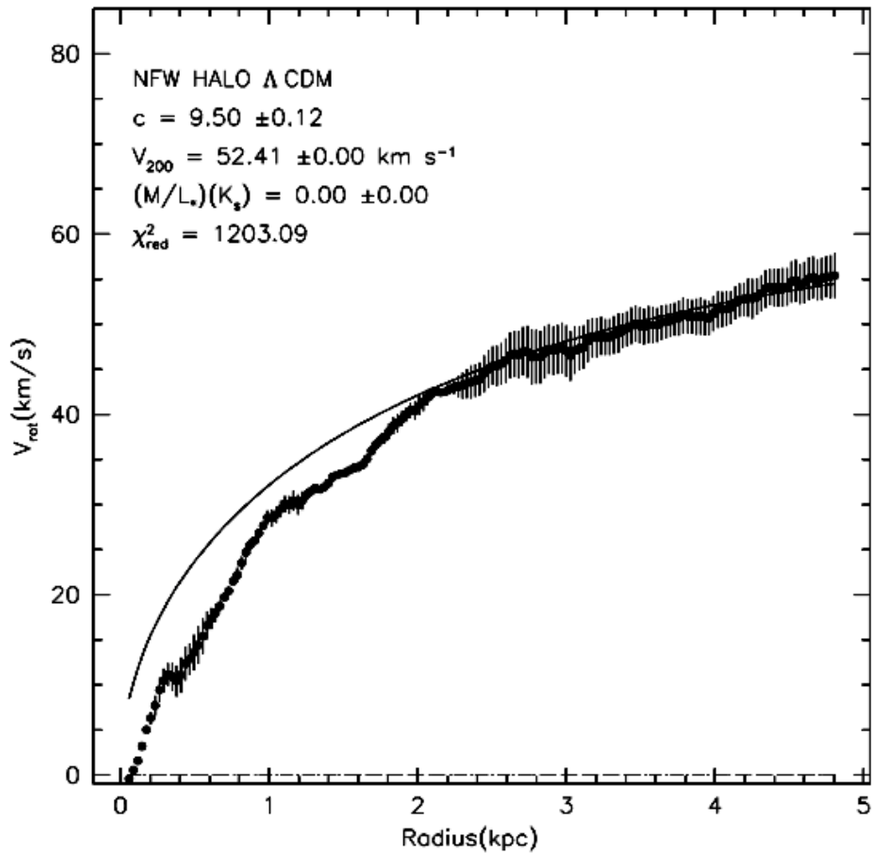

NGC 6822, de Blok etal 2007

Oh et al 2011

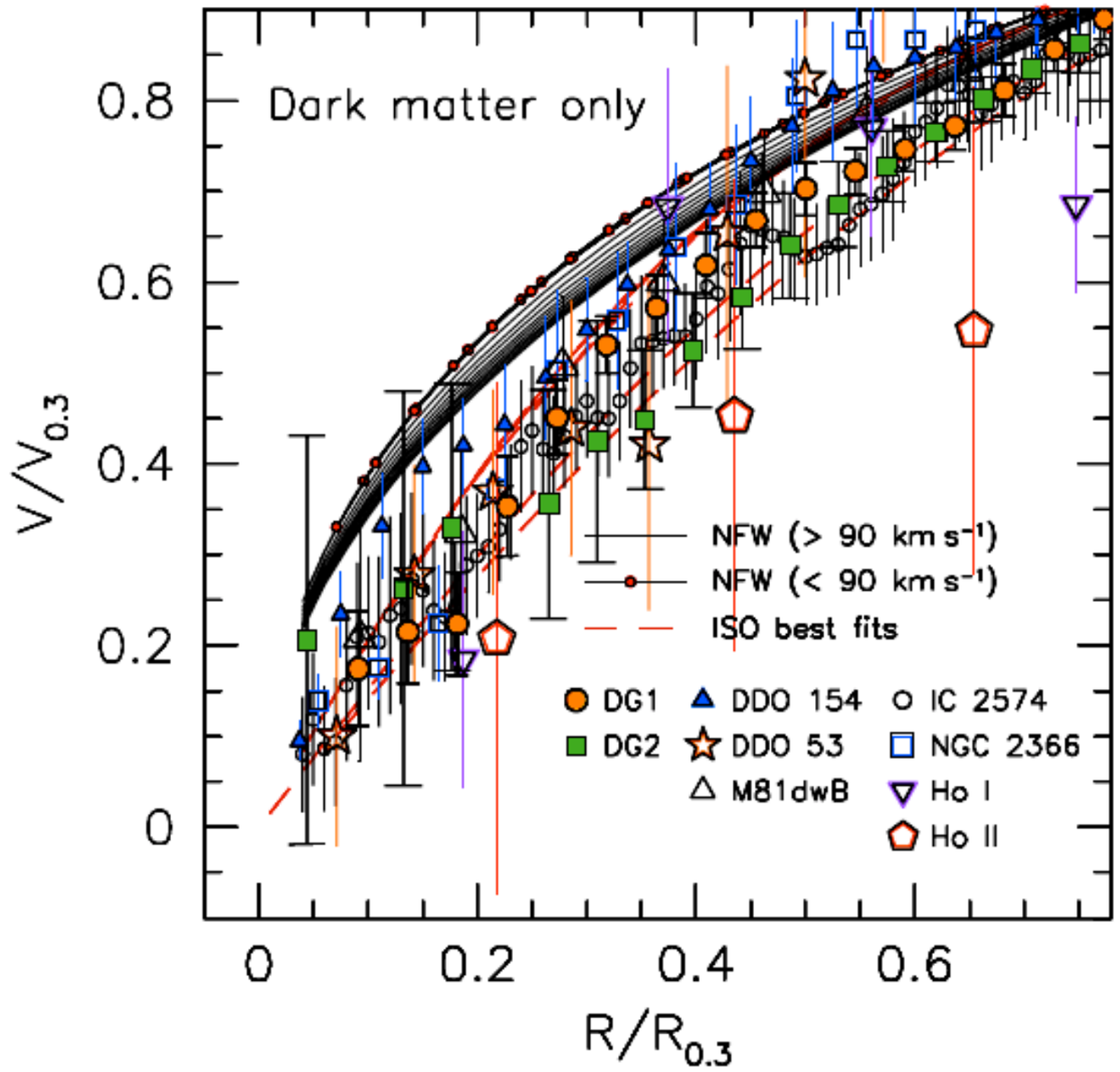

Numerous episodes of baryon infall followed by a strong burst of star formation, which expels the baryons. At the beginning of each episode the baryons dominate the gravitational potential. The DM contracts to respond to the changed potential. A sudden onset of star formation drives the baryons out. The DM also moves out because of the shallower potential. Each episode produces a relatively small effect on the DM, but a large number of them results in a significant decline of the DM density. Indeed, cosmological simulations that implement this process show a strong decline of the DM density. Whether the process happens in reality is still unclear.

Simulations with the cycles of infall-burst-expansion show flattening of the DM cusp may occur. If this happened to our Galaxy, then the DM density within the central ~ 500 pc may become constant. This would reduce the annihilation signal by orders of magnitude. We note that this mechanism would wipe out the DM cusp also in centers of dwarf galaxies.

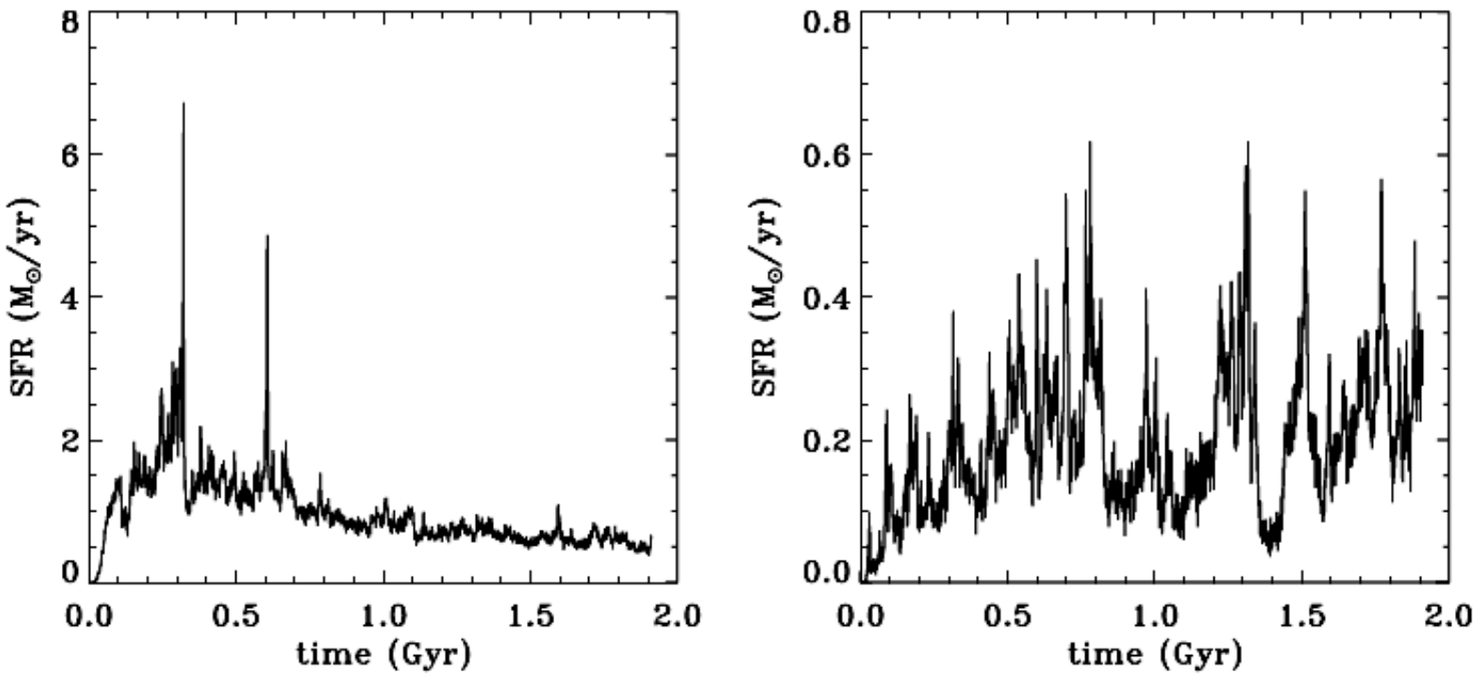

Figure 3. Star formation history in the runs without (left-hand plot) and with (right-hand plot) feedback.

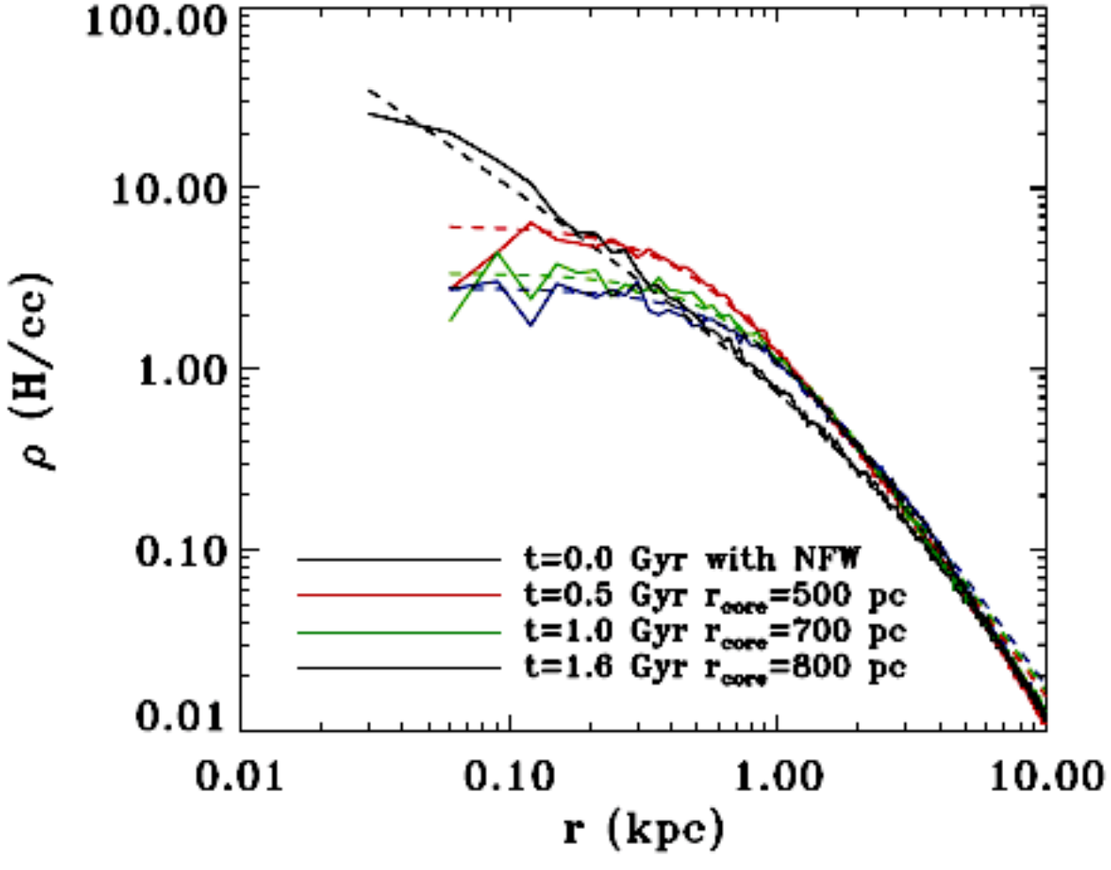

Figure 5. Evolution of the dark matter density profile over the 2Gyr of evolution for the control run with cooling, star formation and stellar feedback. We see the formation of a large core. We also show for comparison the analytical fit (dashed line) based on a pseudo-isothermal profile.

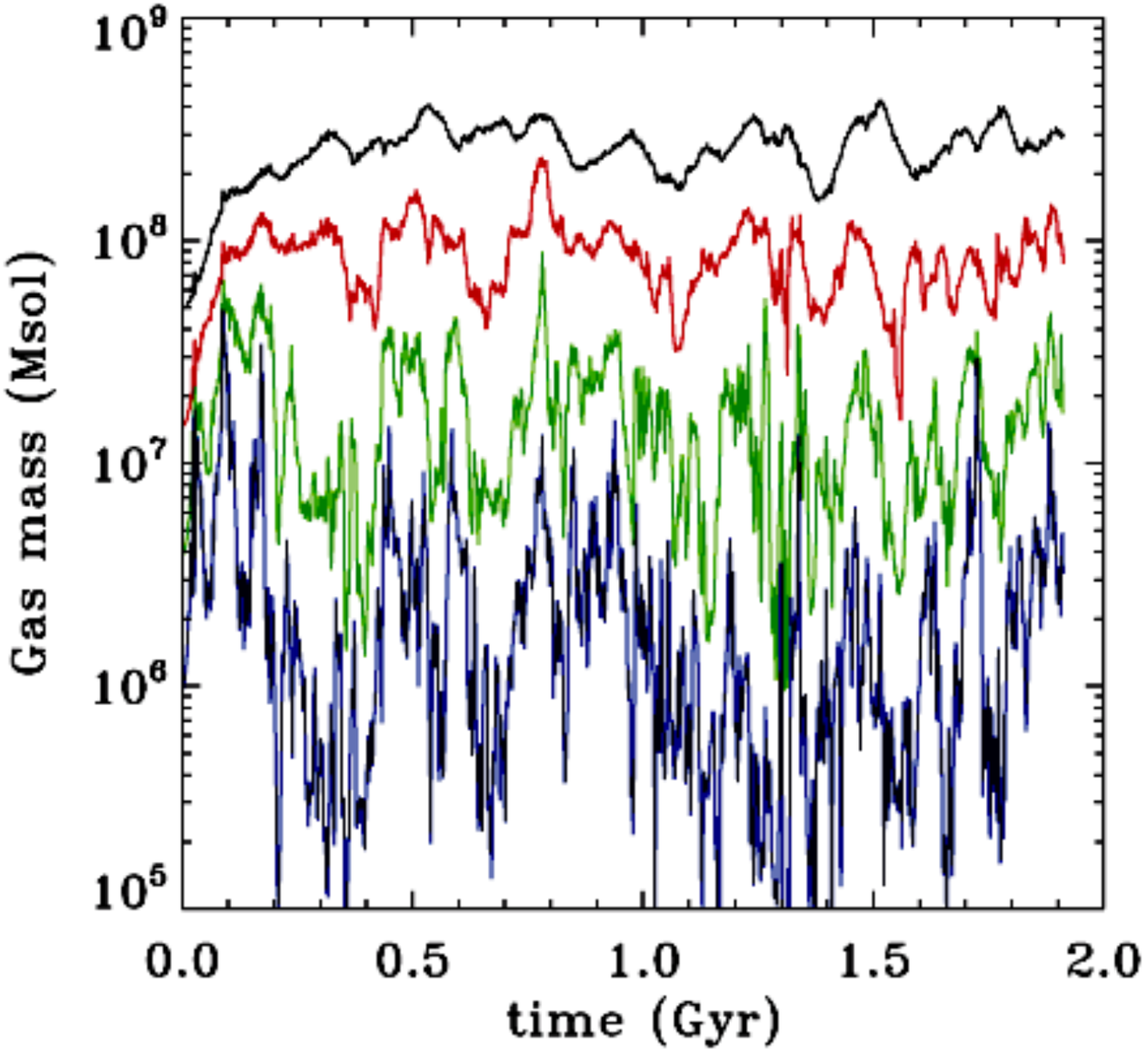

Figure 7. Time evolution of the total enclosed gas mass within spheres of radii 200 (blue), 400 (green), 800 (red) and 1600 (black) pc for the simulation with feedback.

Gamma-ray flux from dark matter annihilation

A heavy ($m_\chi > 1$GeV) particle with a finite annihilation cross section into Standard Model particles would be theoretically well motivated as DM.

The canonical example of such DM is a non-relativistic thermal relic that froze out of equilibrium with the particle bath in the early Universe. While significant annihilation would cease during freeze-out, if the DM pair annihilation is due to an s-wave process and therefore velocity independent, low rates of annihilation would continue to the present day.

Such a DM particle could yield the measured DM energy density today, $\Omega h^2 = 0.1199 \pm 0.0027$, provided the annihilation cross section averaged over the velocity distribution is near $\langle \sigma v \rangle \sim 3 \times 10^{-26}\,\mathrm{cm^3\,s^{-1}}$. This can be realized in models with supersymmetry, though other models can also work.

$$\Omega_{\mathrm{WIMP}} h^2 \sim \frac{3.1 \cdot 10^{-27}}{< \sigma_A |\vec{v}| >}$$

E.Charles et al 2016

Gamma-ray flux from dark matter annihilation

Detection of cosmic gamma rays with the Fermi Space Telescope: 20 MeV - 300 GeV

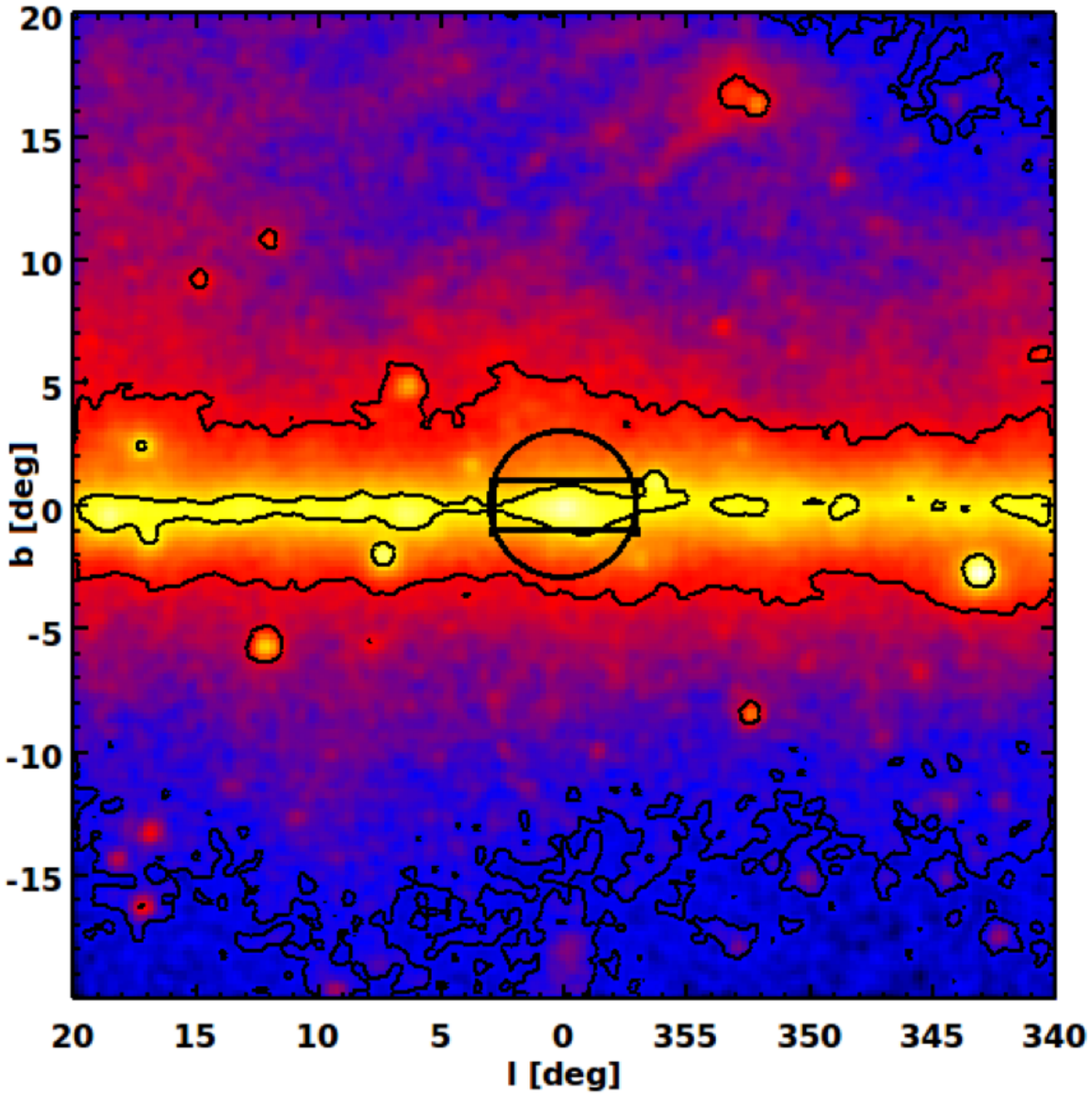

Map of the observed flux by the Fermi -LAT in the energy range 1 − 100 GeV, in units of photons cm−2 s−1

Gamma-ray flux from dark matter annihilation

Astronomical (non-DM) backgrounds: point sources and diffuse

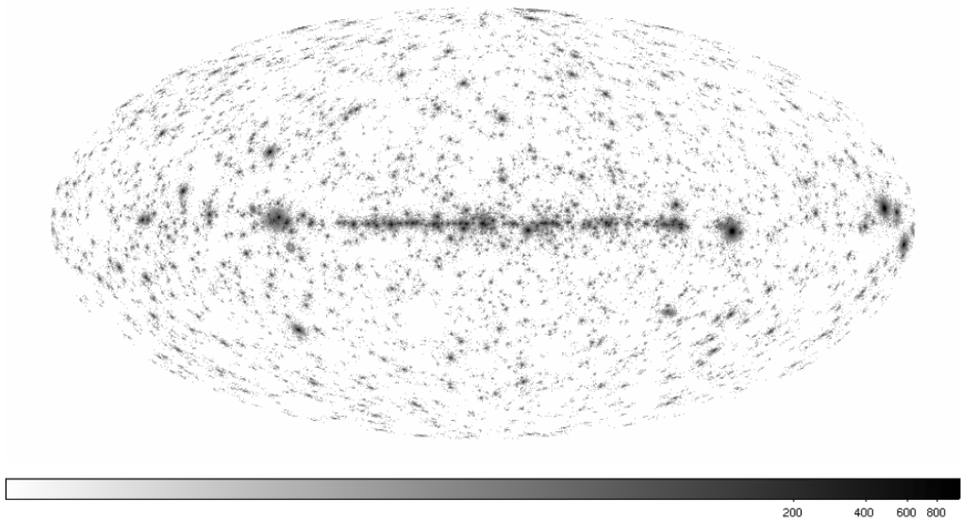

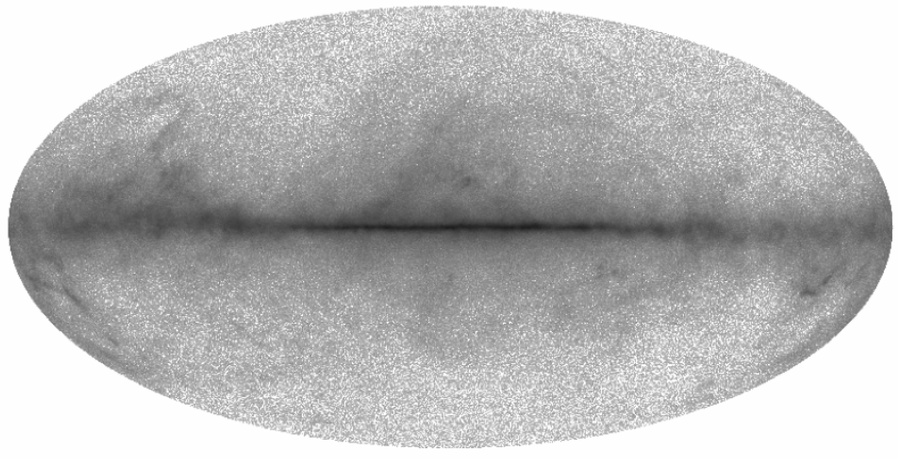

Spectrum of the Galactic center excess in the inner 15 ∘ × 15 ∘ region obtained with four different models of the Galactic diffuse emission compared with spectra obtained from other published analyses based on still-different models of the Galactic diffuse emission.

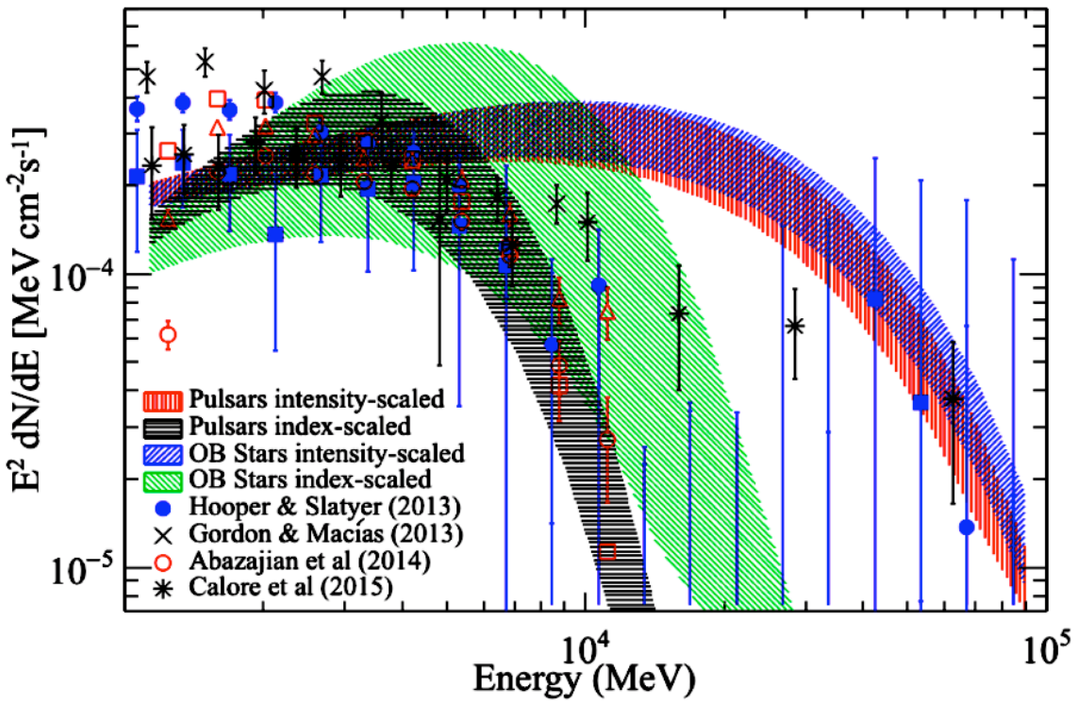

E.Charles et al 2016

Gamma-ray flux from dark matter annihilation: WIMP

The gamma-ray flux from DM annihilation in the Galactic halo has two main contributions:

1) prompt photons and 2) photons induced via Inverse Compton Scattering (ICS).

The former are produced indirectly through hadronization, fragmentation and decays of the DM annihilation products or by internal bremsstrahlung, or directly through one-loop processes (but these are typically suppressed in most DM models).

The second contribution originates from electrons and positrons produced in DM annihilations, via ICS off the ambient photon background. The other two possible contributions to the gamma-ray flux from DM annihilation can be neglected: radiation from bremsstrahlung is expected to be sub-dominant with respect to ICS in the energy range considered (1 - 100 GeV) and a few degrees off the Galactic plane, and synchrotron radiation is only relevant at radio frequencies, below the Fermi-LAT threshold.

annihilation from a given observational region $\Delta\Omega$ in the Galactic halo can be written as follows:

$$\frac{d\Phi_\gamma}{dE_\gamma}(E_\gamma, \Delta\Omega) = \left(\frac{d\Phi_\gamma}{dE_\gamma}\right)_{prompt} + \left(\frac{d\Phi_\gamma}{dE_\gamma}\right)_{ICS}$$

Prompt gamma rays: WIMPs

A continuous spectrum of gamma rays is produced mainly by the decays of π^0's generated in the cascading of annihilation products and also by internal bremsstrahlung. While the former process is completely determined for each given final state of annihilation ($b\bar{b}$, $\tau^+\tau^-$, $\mu^+\mu^-$ and W^+W^- channels), the latter depends in general on the details of the DM model such as the DM particle spin and the properties of the mediating particle.

the prompt contribution can be written as

$$\left(\frac{d\Phi_\gamma}{dE_\gamma}\right)_{prompt} = \sum_i \frac{dN_\gamma^i}{dE_\gamma} \frac{\langle\sigma_i v\rangle}{8\pi m_{DM}^2} \bar{J}(\Delta\Omega)\Delta\Omega$$

The discrete sum is over all DM annihilation channels. dN_γ^i / dE_γ is the differential gamma-ray yield, $\langle\sigma_i v\rangle$ is the annihilation cross-section averaged over the velocitv distribution of the DM particles, m_{DM} is the mass of the DM particle, and th $\bar{J}(\Delta\Omega)$

$$\bar{J}(\Delta\Omega) \equiv \frac{1}{\Delta\Omega}\int d\Omega \int_{l.o.s.} \rho^2(r(l,\Psi))\, dl$$

The J-factor accounts for both the DM distribution and the geometry of the system2. The integral of the square of the DM density ρ^2 in the direction of observation Ψ is along the line of sight (l.o.s), and r and l represent the galactocentric distance and the distance to the Earth, respectively

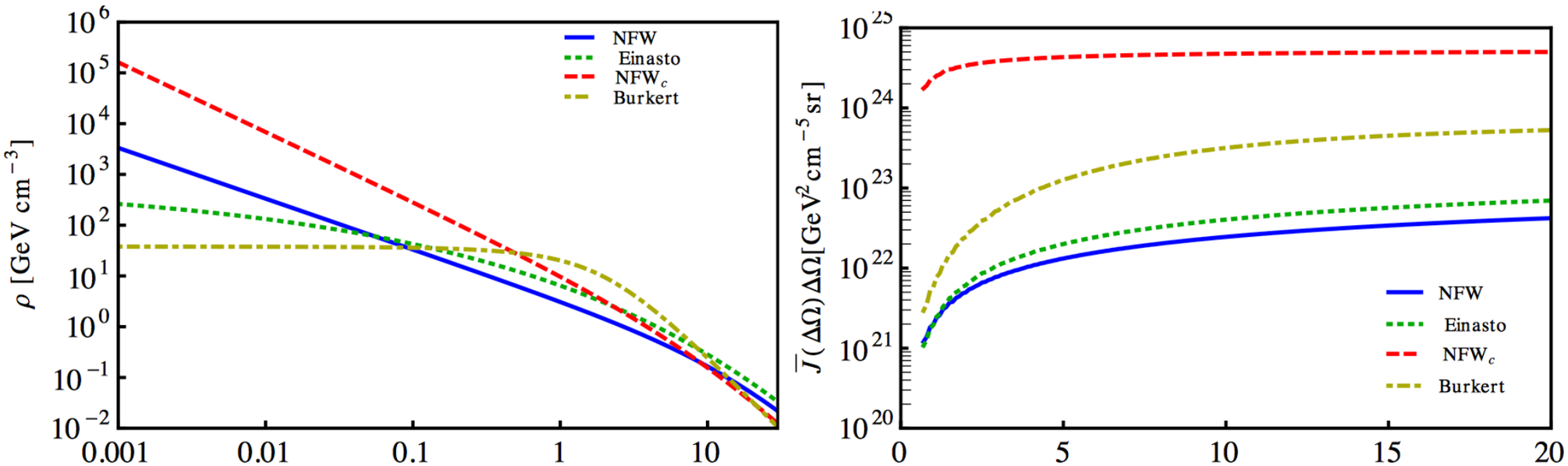

Left panel: DM density profiles

Right panel: The J¯(ΔΩ)ΔΩ quantity integrated on a ring with inner radius of 0.5○ (~ 0.07 kpc) and external radius of Ψ (R⊙ tan Ψ) for the DM density profiles given in Table 1. Blue (solid), red (long-dashed), green (short-dashed) and yellow (dot-dashed) lines correspond to NFW, NFWc = contracted NFW, Einasto and Burkert profiles, respectively. The four DM density profiles are compatible with current observational data.

results can be interpreted in general as implying that vanilla WIMP models and contracted DM profiles are incompatible with the Fermi data.

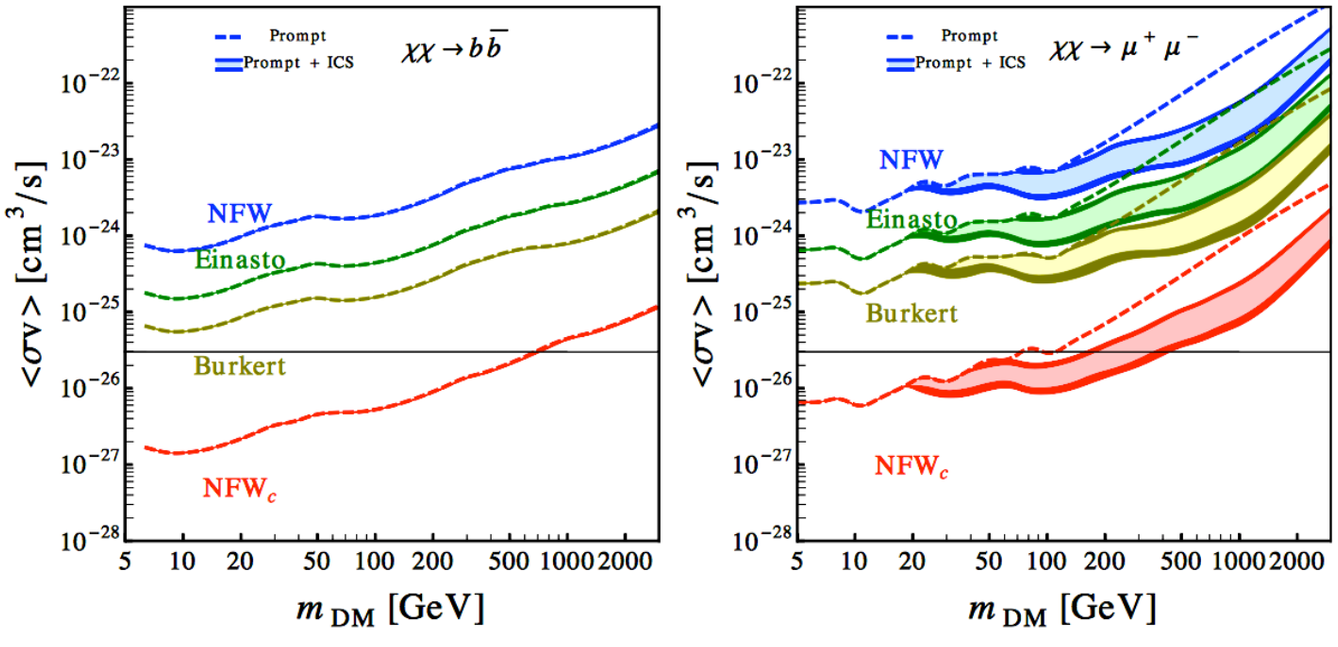

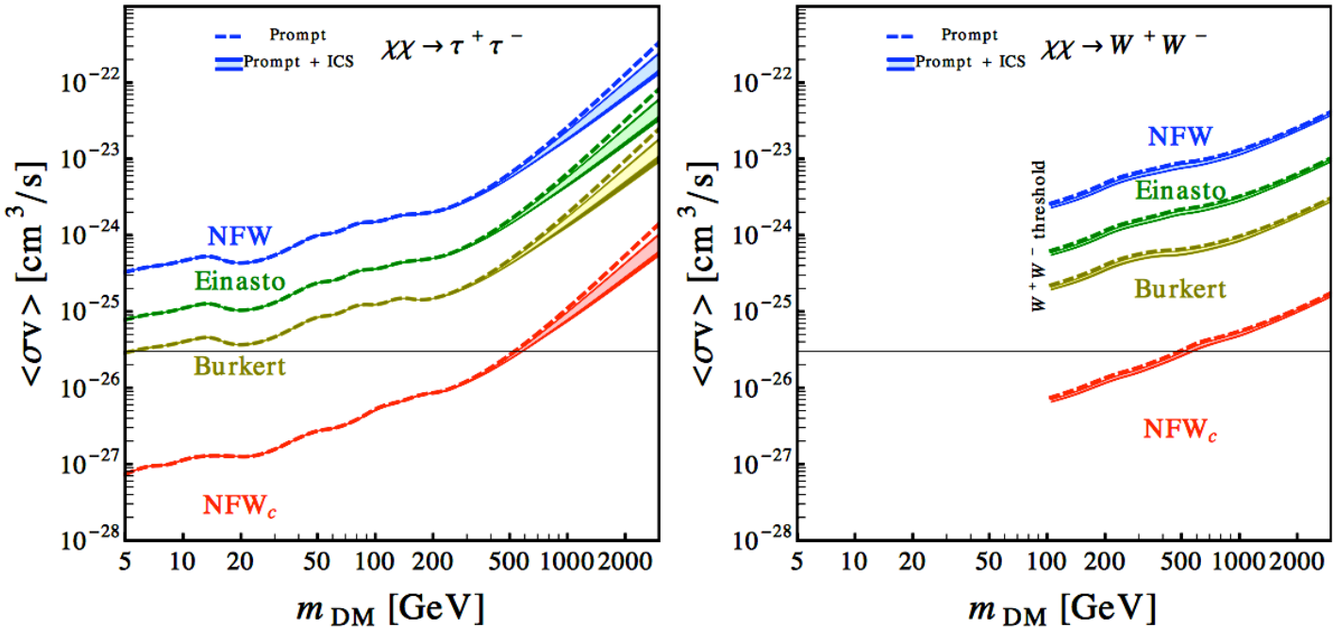

Figure 5: 3σ upper limits on the annihilation cross-section of models in which DM annihilates into $b\bar{b}$, $\mu^+\mu^-$ (upper panel), $\tau^+\tau^-$ or W^+W^- (lower panel), for the four DM density profiles discussed in the text. Upper limits set without including the ICS component in the computation are also given as dashed curves (prompt) for comparison. The uncertainty in the diffusion model is shown as the thickness of the solid curves (from top to bottom: MIN, MED, MAX) while the lighter shaded regions represent the impact of the different strengths of the Galactic magnetic field with lower(higher) values of the cross-section corresponding to $B_0 = 1\ \mu$G($B_0 = 10\ \mu$G). The horizontal line corresponds to the expected value of the thermal cross-section for a generic WIMP candidate.

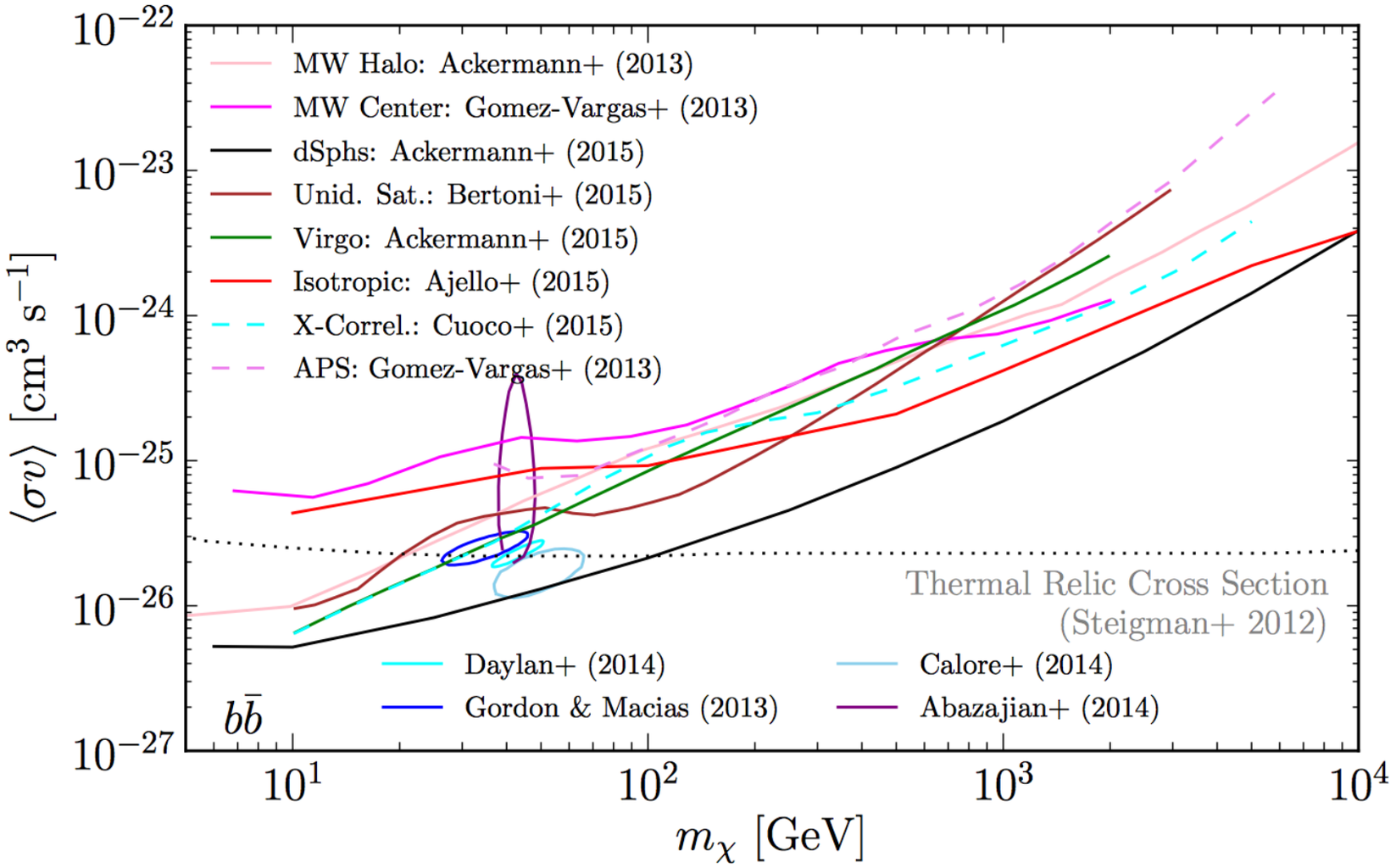

Comparison of representative published limits (curves) and best-fit regions (ellipses) for the $b\bar{b}$ channel found using LAT data for several DM targets.

Spectral Lines

In many DM models, pairs of DM particles can annihilate into a γ ray and a second particle (X), e.g., $\gamma\gamma$, γZ, or γH. Since DM is strongly constrained to be electrically neutral, it has no direct coupling to photons. Thus the process $\chi\chi \to \gamma X$ occurs only through higher-order loops, resulting in a branching fraction that is only $\sim 10^{-4} - 10^{-1}$ [236–240]. If a DM particle annihilates to γX the photons are monochromatic in the rest frame with rest-frame energy

$$E_\gamma = m_\chi \left(1 - \frac{m_X^2}{4m_\chi^2}\right). \tag{9}$$

This would result in a line-like feature in the γ-ray spectrum. Possible evidence of such a line-like feature at 130 GeV strongly correlated with the Galactic center region was reported [57, 241–243], and also seen in nearby galaxy clusters [244], and unassociated LAT sources [245, 246]. The feature was not seen in the vicinity of nearby dwarf galaxies [247]. However such a signal is expected to be much fainter than in the Galactic center. Potential instrumental effects and a similar feature detected in the bright γ-ray emission from cosmic-ray interactions in Earth's upper atmosphere (the Limb) have also been discussed [244, 248, 249]. A systematic investigation of the spatial morphology of the 130 GeV feature and other line-like features in the Galactic plane is presented in [250].

4.9.1. Spectral Lines: Current Status

Since these reports, the LAT Collaboration has searched for spectral lines using both the Pass 7REP [251] and Pass 8 [80] data sets and found that the original putative signal has faded to less than one standard deviation significance ($< 1\sigma$) once the trials factors associated with scanning in DM particles mass from 1 GeV to 500 GeV and for several different ROIs associated with different DM radial profiles, which are

E.Charles et al 2016

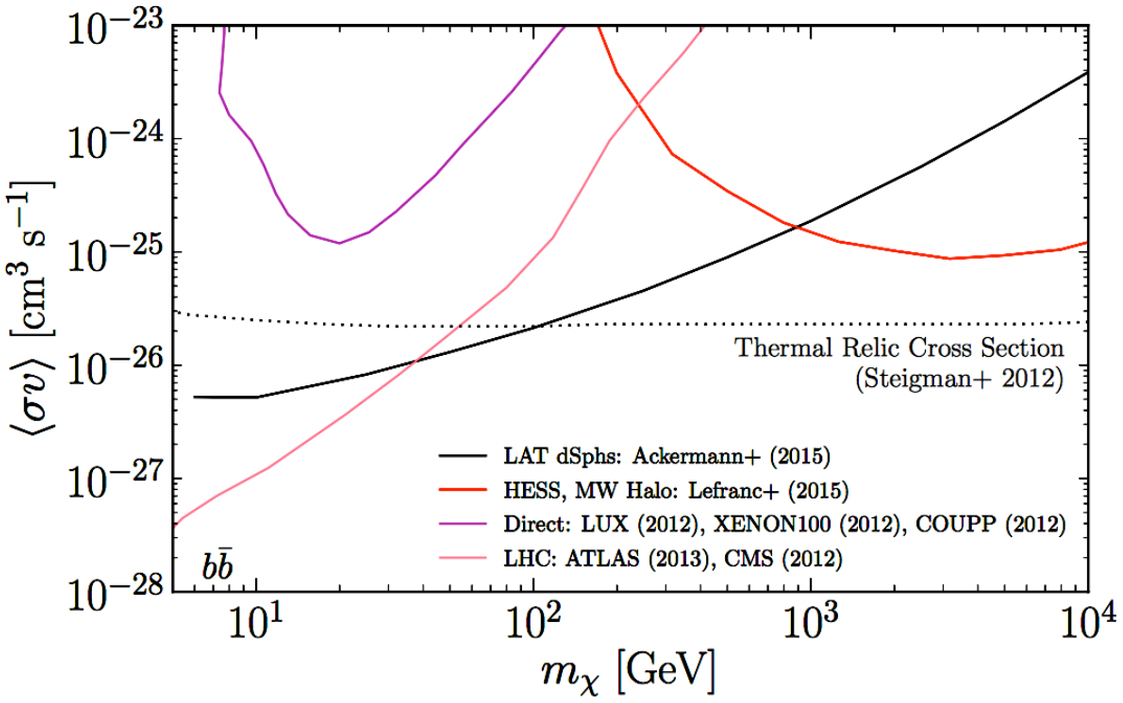

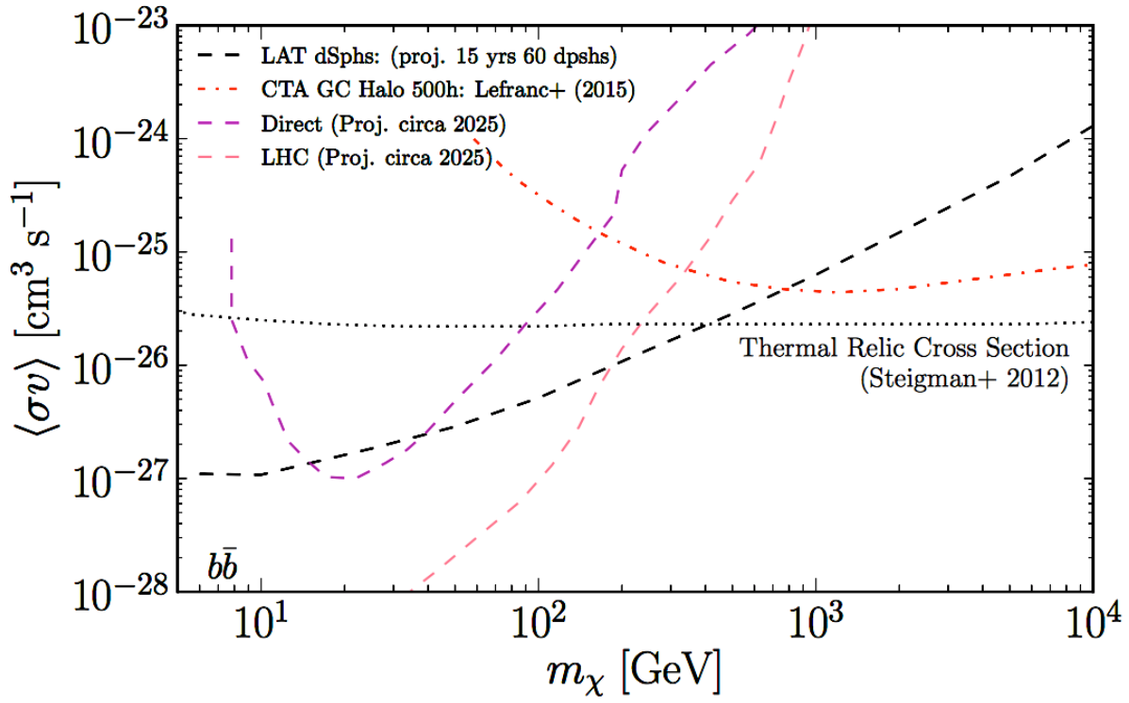

Comparison of best current (left) and projected (right) indirect-detection, direct-detection (spin-dependent) and collider-production limits on $\langle\sigma v\rangle$ in the $b\bar{b}$ channel. Conversion of direct-detection and collider limits to the $\langle\sigma v\rangle$ scale is based on the assumption of four particle contact interactions for the production/annihilation of DM. As noted in the text, this assumption is quite uncertain (potentially by orders of magnitude) and the comparisons shown here should be considered schematic.

E.Charles et al 2016